Computer Physics Communications 182 (2011) 289–298

Contents lists available at ScienceDirect

Computer Physics Communications

www.elsevier.com/locate/cpc

Application of coordinate transformation and finite differences method in numerical modeling of quantum dash band structure

B.M. Stupovski, J.V. Crnjanski, D.M. Gvozdić *

School of Electrical Engineering, University of Belgrade, Bulevar Kralja Aleksandra 73b, P.O. Box 35-54, 11120 Belgrade, Serbia

ARTICLE INFO

Article history:
Received 22 March 2010
Received in revised form 17 September 2010
Accepted 21 September 2010
Available online 25 September 2010

Keywords:
Quantum dashes
Electronic band structure
Coordinate transformation
Finite difference

ABSTRACT

In this paper we propose an efficient and simple method for the band structure calculation of semiconductor quantum dashes. The method combines a coordinate transformation (mapping) based on an analytical function and the finite differences method (FDM) for solving the single-band Schrödinger equation. We explore suitable coordinate transformations and propose those, which might simultaneously provide a satisfactory fit of the quantum dash heterointerface and creation of an appropriate computational domain which encloses the quantum dash structure. After mapping of the quantum dash and the rest of computational domain, the Schrödinger equation is solved by the FDM in the mapped space. For the proposed coordinate transformations, we investigate and analyze applicability, robustness and convergence of the method by varying the FDM grid density and size of the computational domain. We find that the method provides sufficient accuracy, stability and flexibility with respect to the size and shape of the quantum dash and above all, extreme simplicity, which is promising and essential for an extension of the method to the multiband Schrödinger equation case.

1. Introduction

Presently, there is a strong interest in self-assembled semiconductor quantum nanostructures due to their new and advanced electronic and optical properties. From the technological point of view, their significant advantage is self-assembling process of growth, which doesn't require any additional lithographic steps. The most interesting applications of these structures are usually related to semiconductor lasers and optical amplifiers [1–5], where self-assembled quantum nanostructures are used as an active region, providing for low threshold current [6], low chirp and small linewidth enhancement factor [7].

One of the most recent and intriguing representatives of the self-assembled quantum nanostructures are quantum dashes (QDHs), which are wire-like semiconductor nanostructures. The self-assembling growth process leads to an ensemble of QDHs with significant size fluctuation with respect to their widths, heights and lengths [8–10]. The size fluctuation considerably affects the QDHs band structure and consequently electronic and optical characteristics [2,8,11,12]. In order to theoretically analyze an ensemble of QDHs it is important to develop an efficient, accurate and simple method for the band structure calculation, which can handle arbitrary profile of a single QDH.

Although there is a group of methods (e.g. empirical pseudopotential method, tight-binding method [13,14], etc.) which can be used for calculation of the QDH band structure by including the potentials of individual atoms, these methods are computationally very demanding. The more efficient method, which has been widely used during several decades, is the envelope function approximation (EFA). An essential assumption in the derivation of the EFA is that potential is slowly varying on the scale of the lattice constant. The advantage and numerical efficiency of the EFA come from the fact that one can avoid the explicit inclusion of the cell periodic potential and that only the slowly varying perturbation enters the Hamiltonian. In this case, the Schrödinger equation involves the slowly varying part of the wavefunction.

The most commonly used numerical method for implementation of the EFA in calculation of the band structure for one- and zero-dimensional irregular nanostructures is the finite element method (FEM) [15–17]. This method provides high flexibility and it can be implemented even when heterointerfaces are such that it is difficult to describe them by analytical functions. Since basis functions in the FEM are relatively simple, the discretization matrix can be easily set and efficiently evaluated. Although, in this case, the discretization matrix is sparse, its size is usually very large, depending on the computational domain size and the mesh density. However, the major drawback of the FEM is that in addition it requires specialized routines for automatic or manual mesh generation. The mesh itself, if not carefully generated, can affect the accuracy of the calculation and lead to unnecessarily large discretization matrices and eigenvalue problems.

* Corresponding author. Tel.: +381 11 3370 060; fax: +381 11 324 8681.
E-mail address: gvozdic@etf.rs (D.M. Gvozdić).

0010-4655/$ – see front matter
doi:10.1016/j.cpc.2010.09.014

On the other hand, the expansion methods [18–20] are more suitable for Hamiltonians which complexity overcomes the simple elliptic interface problems. Good examples of complex Hamiltonians are those implemented in the multiband Schrödinger equation [18,20] or those which include bulk-inversion-asymmetry terms [21]. The size of the Hamiltonian matrix for the expansion methods depends on the quality and number of basis functions involved in the expansion. However, the density of Hamiltonian matrices is usually large and does not depend significantly on the Hamiltonian complexity, making the method suitable for complex Hamiltonians. Although, these Hamiltonian matrices might be of moderate size, due to their large density, they require long computational time for the diagonalization, which is usually proportional to the third power of the matrix size. In addition to that, evaluation of the Hamiltonian matrix may take a lot of computational power if it is performed by numerical integration.

The method which is generally very popular due to its simplicity, even in the case of complex Hamiltonians, and which provides a high order convergence rate and sparse discretization matrices, is the finite differences method (FDM) [22]. However, the FDM in principle requires that the heterointerfaces are flat or polygonal, since otherwise they may not be aligned with the grid, but rather crossing between the grid points, causing low approximation accuracy [23]. This limits the class of problems which can be considered by the FDM. From that point of view, the band structure analysis of nanostructures such as quantum dots and dashes might look beyond capabilities of the FDM, since their shape is rarely described by flat heterointerfaces, but rather with various lens-like curves.

It is well known that in some cases coordinate transformations may simplify geometry of the structure and computational domain, leading to the flat interfaces of the structure and computational domain, and enabling implementation of the FDM within a new coordinate space [24–26]. In the case of nanostructures where confinement is two dimensional (2D), the most efficient coordinate transformations are based on conformal mapping [19], since the kinetic part of the Hamiltonian in the mapped space has the form of the Laplacian multiplied by the determinant of the Jacobian matrix, while the mixed derivatives do not appear in the Hamiltonian. On the other hand, in some cases, the computational domain may consist of several subdomains [25], requiring more than one function to achieve flat boundaries in the mapped space. In these cases, the subdomains must be cautiously connected in order to avoid the loss of accuracy, requiring additional programming efforts. Moreover, the flat computational domain obtained after mapping, might be of inadequate size with respect to the wavefunction distribution or grid density. In other words, the equidistant grid in the mapped space may correspond to a dense grid in the region of the original space where the wavefunction changes relatively slowly, while a coarse grid may cover the region characterized by rapid change of the wavefunction, affecting in such a manner the accuracy of calculation. Similarly, it may happen that a large computational domain in the mapped space corresponds to a small domain in the original space, insufficient to accommodate the wavefunctions. However, a large computational domain in the mapped space may lead to the huge discretization matrices, which are demanding for the diagonalization or which, in spite of their size, may not provide a sufficient accuracy of the calculated eigenenergies.

In this paper, we propose a numerical method based on the combination of coordinate transformation and the FDM, which provides an efficient and simple approach for the band structure and wavefunction calculations of quantum dash nanostructures, with various cross-section shapes, widths and heights. We focus our research on the quality of the coordinate transformation with respect to simultaneous heterointerface fitting and definition of the computational domain. In other words, we search for mappings which can provide suitable computational domains, sufficient to accommodate wavefunctions, and simultaneously enabling successful fitting of the well-barrier heterointerface. A special attention is given to QDHs with the lens-like cross-section profile representing the most frequently adopted approximation for the QDH shape [4,12,27]. However, we additionally extend our approach to the case in which the QDH cross-section profile can be approximated with a trapezoidal shape [10,28,29].

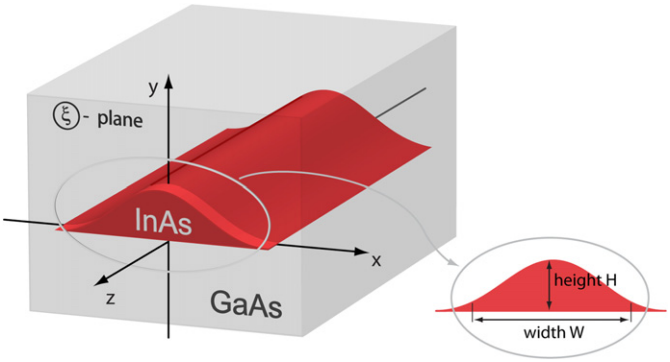

Fig. 1. (Color online.) Schematic of InAs lens-like quantum dash embedded in GaAs infinite host matrix.

In Section 2 we define geometry of the quantum dash profile and based on it, we present the theory behind the numerical method. In Section 3 we consider the most important features which have to be satisfied by the coordinate transformation and propose several possible fitting solutions for different profiles of QDH cross-sections. In Section 4, we investigate the influence of the discretization step and domain size on the convergence of the method and investigate two coordinate transformations for two different QDH profiles. Finally, in Section 5 we present our conclusions.

2. Description of the method

In order to give a detailed description of the theory behind our numerical method, we shortly discuss and analyze geometrical and compositional structure of a single QDH based on InAs well material, which is embedded in GaAs host matrix (cf. Fig. 1). The effective mass for InAs ($m^*_{\mathrm{InAs}} = 0.0221m_0$) and GaAs ($m^*_{\mathrm{GaAs}} = 0.0623m_0$), as well as the conduction band offset ($\Delta E_c = 858.7$ meV), are taken from [30], where m_0 is the free electron mass. Since QDH is an elongated InAs island [9], the well material has almost a quantum-wire nature. Therefore, the band structure of the QDH is mainly dependent on the two-dimensional (2D) carrier confinement in the transversal direction (xy plane in Fig. 1). This confinement, on the other hand, is defined by the profile of QDH cross-section. The most common geometrical approximation of the QDH's cross-section is the lens-like profile [4,12,27], which is shown in Fig. 1. The profile may slightly differ from the lens-like shape depending on the material system and growth conditions. Other common shapes used for the profile approximation are triangular [2,31,32], trapezoidal [10,28,29] and rectangular [8,33,34]. In the case of rectangular and triangular shapes, the FDM can be directly applied, without using the coordinate transformation [23]. The coordinate transformations proposed in our paper are capable to fit lens- and trapezoidal-like shapes. It should be noted that there are more sophisticated coordinate transformations, which can additionally include wetting layer into computation, but they will be considered elsewhere.

The method proposed in this paper consists of four major steps:

1. Selection of a coordinate transformation, which can provide satisfactory fit of the well-barrier heterointerface and size of the computational domain.
2. Mapping of the Hamiltonian into new coordinate space by using the Jacobian matrix for the selected coordinate transformation.
3. The Hamiltonian discretization according to the finite differences scheme and setting of the discretization matrix.
4. Evaluation of the eigenvalues representing the bound states in the QDH. This is done by using specialized routines for eigenvalue computation (LAPACK).

Before we deal with a deeper investigation of suitable coordinate transformations and their features (step 1), we give description of the Hamiltonian mapping and the FDM discretization (steps 2 and 3). We start from the EFA Schrödinger equation for electrons in the conduction band:

$$-\frac{\hbar^2}{2}\left[\frac{\partial}{\partial x}\left(\frac{1}{m^*}\frac{\partial\psi}{\partial x}\right)+\frac{\partial}{\partial y}\left(\frac{1}{m^*}\frac{\partial\psi}{\partial y}\right)\right]+\left[\frac{\hbar^2k_z^2}{2m^*}+U\right]\psi=E\psi, \tag{1}$$

where $\psi=\psi(x,y)$ is the slowly varying part of the total wavefunction, $U=U(x,y)$ is the 2D potential profile determined by the QDH's cross-section and the conduction band offset, $m^*=m^*(x,y)$ is the electronic effective mass, while E is the confinement energy, referenced to the conduction band edge of the QDH barrier material. Due to the elongated geometry of the QDH, the quantization in the longitudinal direction (z-direction) leads to a quasi-continuous subband structure, the energy of which is well approximated with parabolic dependence on corresponding wavevector (k_z). In our analysis we are interested in eigenenergies corresponding to the subband bottom, for which $k_z=0$.

By imposing the continuity of the probability density and the probability current, it is shown that $\psi(x,y)$ and its gradient perpendicular to the interface divided by the effective mass, must be continuous at the material heterointerfaces. Since we implement the finite differences scheme, the boundary conditions are naturally built in into the discretization and need not be enforced explicitly.

Once the coordinate transformation $x=x(u,v)$, $y=y(u,v)$ is chosen, where $\xi=\xi(x,y)$ represents the old coordinate space, the Schrödinger equation can be mapped into new $w=w(u,v)$ space:

$$\begin{aligned}-\frac{\hbar^2}{2}\Bigg[&u_x\frac{\partial}{\partial u}\left(\frac{u_x}{m^*}\frac{\partial\psi}{\partial u}+\frac{v_x}{m^*}\frac{\partial\psi}{\partial v}\right)+v_x\frac{\partial}{\partial v}\left(\frac{u_x}{m^*}\frac{\partial\psi}{\partial u}+\frac{v_x}{m^*}\frac{\partial\psi}{\partial v}\right)\\&+u_y\frac{\partial}{\partial u}\left(\frac{u_y}{m^*}\frac{\partial\psi}{\partial u}+\frac{v_y}{m^*}\frac{\partial\psi}{\partial v}\right)+v_y\frac{\partial}{\partial v}\left(\frac{u_y}{m^*}\frac{\partial\psi}{\partial u}+\frac{v_y}{m^*}\frac{\partial\psi}{\partial v}\right)\Bigg]\\&+U\psi=E\psi.\end{aligned} \tag{2}$$

In Eq. (2) $\psi[x(u,v),y(u,v)]=\psi(u,v)$, $U[x(u,v),y(u,v)]=U(u,v)$, while u_x, v_x, u_y, and v_y are the elements of the Jacobian matrix J_{xy} representing partial derivatives of the inverse functions $u=u(x,y)$ and $v=v(x,y)$ with respect to x and y. Since we want to set the Schrödinger equation in the w-space we need elements of J_{xy} matrix to be expressed as functions of u and v, i.e. $u_x=u_x(u,v)$, $v_x=v_x(u,v)$, $u_y=u_y(u,v)$, $v_y=v_y(u,v)$. Thus, we start from the transformation $x=x(u,v)$, $y=y(u,v)$ and its corresponding Jacobian matrix J_{uv}, which is explicit function on u and v given by:

$$J_{uv}=\begin{bmatrix}x_u & x_v\\ y_u & y_v\end{bmatrix}, \tag{3}$$

where subscripts denote the partial derivatives with respect to u and v. As the Jacobian matrix J_{xy} for the inverse mapping $u=u(x,y)$, $v=v(x,y)$ is given by $J_{xy}=J_{uv}^{-1}$, we finally derive J_{xy} as:

$$J_{xy}=\begin{bmatrix}u_x & u_y\\ v_x & v_y\end{bmatrix}=\begin{bmatrix}x_u & x_v\\ y_u & y_v\end{bmatrix}^{-1}, \tag{4}$$

which is now an explicit function on u and v.

The elements of matrix J_{xy} depend on the selected coordinate transformation. The general form of the transformation used for fitting the heterointerface and definition of the computational domain is given by:

$$x=Cu, \tag{5a}$$

$$y=Cf(u,v), \tag{5b}$$

where C is a scaling factor, expressed in nanometers. This type of coordinate transformation leads to simpler forms of the Jacobian matrices J_{uv} and J_{xy}:

$$J_{uv}=\begin{bmatrix}x_u & x_v\\ y_u & y_v\end{bmatrix}=\begin{bmatrix}C & 0\\ Cf_u & Cf_v\end{bmatrix}, \tag{6a}$$

$$J_{xy}=\begin{bmatrix}u_x & u_y\\ v_x & v_y\end{bmatrix}=\begin{bmatrix}1/C & 0\\ -f_u/(Cf_v) & 1/(Cf_v)\end{bmatrix}=\frac{1}{C}\begin{bmatrix}1 & 0\\ \mu & \rho\end{bmatrix}, \tag{6b}$$

where f_u and f_v are derivatives of $f(u,v)$ with respect to u and v, respectively, $\mu=\mu(u,v)=C\cdot v_x=-f_u/f_v$ and $\rho=\rho(u,v)=C\cdot v_y=1/f_v$. It is important to note that function $f(u,v)$ is such that the determinant of the Jacobian matrix is different than 0, i.e. $|J_{uv}|=|J_{xy}|^{-1}=C^2\cdot f_v\neq 0$. In this case, the transformation is "one to one" in the neighborhood of a point and it has the inverse transformation in all domain points. In the case of transformation given by (5), Eq. (2) is simplified and becomes:

$$\begin{aligned}-\frac{\hbar^2}{2C^2}\Bigg[&\frac{\partial}{\partial u}\left(\frac{1}{m^*}\frac{\partial\psi}{\partial u}+\frac{\mu}{m^*}\frac{\partial\psi}{\partial v}\right)+\mu\frac{\partial}{\partial v}\left(\frac{1}{m^*}\frac{\partial\psi}{\partial u}+\frac{\mu}{m^*}\frac{\partial\psi}{\partial v}\right)\\&+\rho\frac{\partial}{\partial v}\left(\frac{\rho}{m^*}\frac{\partial\psi}{\partial v}\right)\Bigg]+U\psi=E\psi.\end{aligned} \tag{7}$$

If we use standard central differences, we can discretize Eq. (7) as follows:

$$\begin{aligned}-\frac{\hbar^2}{2C^2}\Bigg\{&\frac{1}{h_u}\Bigg[\left(\frac{1}{m^*}\right)_{i+1/2,j}\frac{\psi_{i+1,j}-\psi_{i,j}}{h_u}-\left(\frac{1}{m^*}\right)_{i-1/2,j}\\&\times\frac{\psi_{i,j}-\psi_{i-1,j}}{h_u}+\left(\frac{\mu}{m^*}\right)_{i+1/2,j}\frac{\psi_{i+1/2,j+1/2}-\psi_{i+1/2,j-1/2}}{h_v}\\&-\left(\frac{\mu}{m^*}\right)_{i-1/2,j}\frac{\psi_{i-1/2,j+1/2}-\psi_{i-1/2,j-1/2}}{h_v}\Bigg]\\&+\frac{(\mu)_{i,j}}{h_v}\Bigg[\left(\frac{1}{m^*}\right)_{i,j+1/2}\frac{\psi_{i+1/2,j+1/2}-\psi_{i-1/2,j+1/2}}{h_u}\\&-\left(\frac{1}{m^*}\right)_{i,j-1/2}\frac{\psi_{i+1/2,j-1/2}-\psi_{i-1/2,j-1/2}}{h_u}\\&+\left(\frac{\mu}{m^*}\right)_{i,j+1/2}\frac{\psi_{i,j+1}-\psi_{i,j}}{h_v}-\left(\frac{\mu}{m^*}\right)_{i,j-1/2}\frac{\psi_{i,j}-\psi_{i,j-1}}{h_v}\Bigg]\\&+\frac{(\rho)_{i,j}}{h_v}\Bigg[\left(\frac{\rho}{m^*}\right)_{i,j+1/2}\frac{\psi_{i,j+1}-\psi_{i,j}}{h_v}\\&-\left(\frac{\rho}{m^*}\right)_{i,j-1/2}\frac{\psi_{i,j}-\psi_{i,j-1}}{h_v}\Bigg]\Bigg\}+U_{i,j}\psi_{i,j}=E\psi_{i,j},\end{aligned} \tag{8}$$

Table 1
A set of functions $g(u), h(v)$, and $\gamma(v)$ which satisfy conditions required for coordinate transformation, where n, m and p are positive integers.

Suggested functions for $g(u)$: $(G + B \cdot u^{2m})^{-1}$; $\exp(-B \cdot u^{2m})$; $\mathrm{sech}(B \cdot u^{m})$; $\mathrm{sech}(G + B \cdot u^{2m})$
Suggested functions for $h(v)$: v^{2n+1}; $\sinh(A \cdot v^{2n+1})$
Suggested functions for $\gamma(v)$: $(F + K \cdot v^{2p})^{-1}$; $\mathrm{sech}(K \cdot v^{p})$; $\mathrm{sech}(F + K \cdot v^{2p})$

where i and j denote indices of the discretization points, while h_u and h_v are discretization steps, along u and v coordinate, respectively. It can be seen from Eq. (8) that the implemented discretization method preserves continuity of the probability density and the probability current, since the effective masses remain under the derivative. By imposing the Dirichlet boundary conditions at the boundary of the computational domain, where the wavefunction is equal to zero, we evaluate the discretization matrix by using relation (8). It is important to note that for an accurate calculation of eigenenergies the effective mass at mid-points ($i + 1/2$ or $j + 1/2$) has to be calculated as an average of the effective masses in adjacent points, rather than the average of their reciprocal values, as one may expect by inspection of relation (8).

3. Coordinate transformation

There are several coordinate transformations which can fit the heterointerfaces of the QDH shown in Fig. 1. Thus we can consider $f(u, v)$ as a family of functions. This family is not uniquely defined, but rather has to fulfill certain conditions. Although transformations defined by the function family may lead to similar cross-section profiles, they may differ significantly depending on the fitting parameters defining function $f(u, v)$. It means that in spite of the fact that functions are not the same, for properly adopted fitting parameters, they provide same or similar cross-section profiles. Having in mind the profile of the QDH, it is obvious that in order to fit the well-barrier heterointerface, $f(u, v)$ has to be Gaussian-like with respect to u, i.e. an even function, decaying with $|u|$ and with the maximum at $u = 0$. On the other hand, for the outer dash region, i.e. the barrier, $f(u, v)$ has to provide similar profile as for the well-barrier heterointerface, which for larger $|v|$, has to be wider with respect to u, and enabling, in such a way, enclosure of the QDH structure and determination of the computational domain. This reasoning leads to possible solutions for the function $f(u, v)$, which can be represented as a product of two functions, where one depends on u and the other on v, i.e. $f(u, v) = h(v) \cdot g(u)$. In $f(u, v)$, $g(u)$ is a Gaussian-like function, while $h(v)$ is any odd function, which modulo is monotonically increasing with $|v|$. In such a manner, $h(v)$ modulates the magnitude of $g(u)$, and enables enlargement of the domain which surrounds the well material of the QDH, either for positive and negative values of v. The description of functions $h(v)$ and $g(u)$ offers several possible solutions and some of them are given in Table 1, where A, B, G, n and m are fitting parameters.

Fig. 2 shows various profiles, which can fit the QDH heterointerface, obtained as combination of the first three functions $g(u)$ and function $h(v) = \sinh(A \cdot v)$. However, the most of the proposed solutions lead to domains which size, for large u, very slowly or almost negligibly increases with $|v|$, causing rapid shrinking of the computational domain, for which $y(u, v) \approx 0$. As a matter of fact, this shrinking is suitable for the fitting of the upper QDH heterointerface, but not for the computational domain. The requirement for a relatively opened computational domain in the x-direction comes from the fact that wavefunctions may significantly "spill out" in the vicinity of the QDH corners, where the upper and

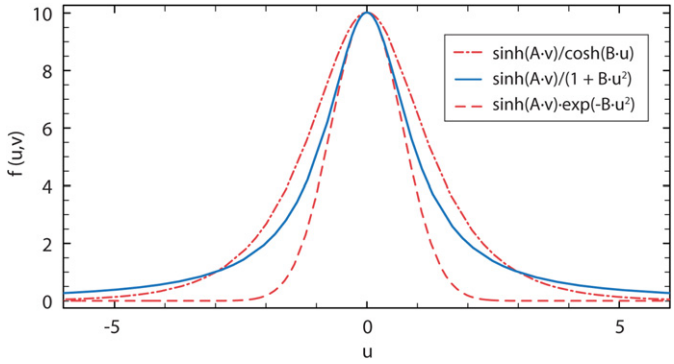

Fig. 2. (Color online.) The Gaussian-like cross-section profiles obtained for some combinations of the functions $h(v)$ and $g(u)$ given in Table 1, and for $v = 2.5$, $A = 1.2$, $B = G = 1$, $C = 1$ nm and $m = 1$.

lower heterointerface join. Thus, it is necessary to preserve suitable Gaussian-like features of the function $g(u)$ and to add a new one, which reduces decay of the function $g(u)$, preventing collapse of the computational domain for large u. This can be achieved by introducing an additional, even function $\gamma(v)$, which monotonically decays with respect to $|v|$ and modulates the argument of function $g(u)$, reducing it for larger $|v|$. Finally, we end up with the function $f(u, v) = h(v) \cdot g[\gamma(v) \cdot u^q]$, where q stands for $2m$ or m, while m is a positive integer. Since the function $\gamma(v)$ has the same features as the function $g(u)$ proposed in Table 1, $g(u)$ can be used as a model for the function $\gamma(v)$. According to Table 1, $\gamma(v)$ is derived from $g(u)$, after parameters G, B and m in the function $g(u)$ are replaced with F, K and p, respectively.

Starting from the previous consideration, we construct a simple coordinate transformation, which provides fit for the lens-like cross-section profile of the QDH and a reasonably small computational domain, which can accommodate the wavefunctions of the bound states:

$$x = Cu, \tag{9a}$$

$$y = \frac{C \sinh(Av)}{\cosh[Bu/\cosh(Kv)]}. \tag{9b}$$

In Fig. 3 we show how each of the parameters in coordinate transformation (9) influence the shape of the function $f(u, v)$, for a fixed value of $v = 3.5$. It can be seen that A affects the maximum of the curve, which exponentially increases with A, while B and K control the width of the Gaussian-like shape. An increase in B leads to decrease in the curve width, while the increase in K leads to its increase. Moreover, the curve shape and its width are more dependent on K than on B. Since $f(u, v)$ depends on the products $A \cdot v$ and $K \cdot v$, the previous consideration indicates that for a fixed A and K, an increase in v is equivalent to the increase in A and K for a fixed v. Thus, the increase in v simultaneously increases the maximum of the curve and its width, allowing expansion of the computational domain for large $|u|$. It means that the chosen function enables successful fitting of the upper QDH heterointerface, while for a larger $|v|$ leads to a wider curve which might represent the boundary of the computational domain.

However, the excellent fitting features of the chosen function (9) do not necessarily correlate with the function invertibility. As it is mentioned in the previous chapter, these features depend on the Jacobian determinant, which has to be different from zero at all points of the computational domain. Thus, we need to analyze the elements of the Jacobian matrix J_{uv}, especially $y_v = y_v(u, v)$, which in this case, represents the Jacobian determinant (cf. Eq. (6a)) divided by C:

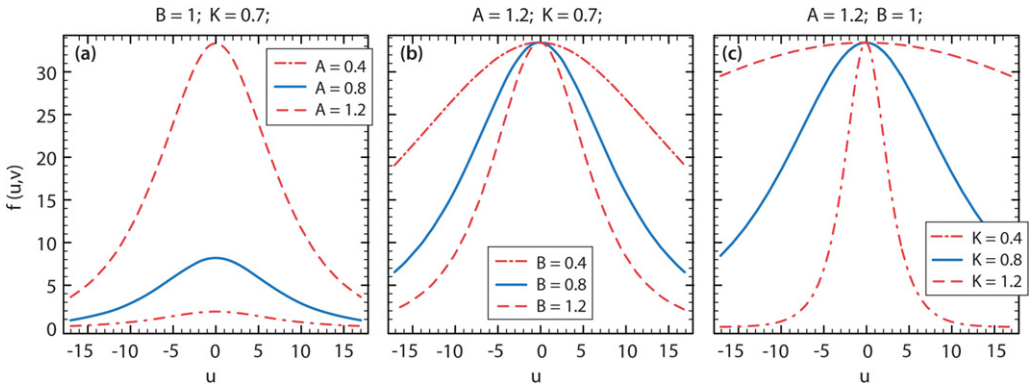

Fig. 3. (Color online.) Influence of the fitting parameters on the coordinate transformation given by relation (9).

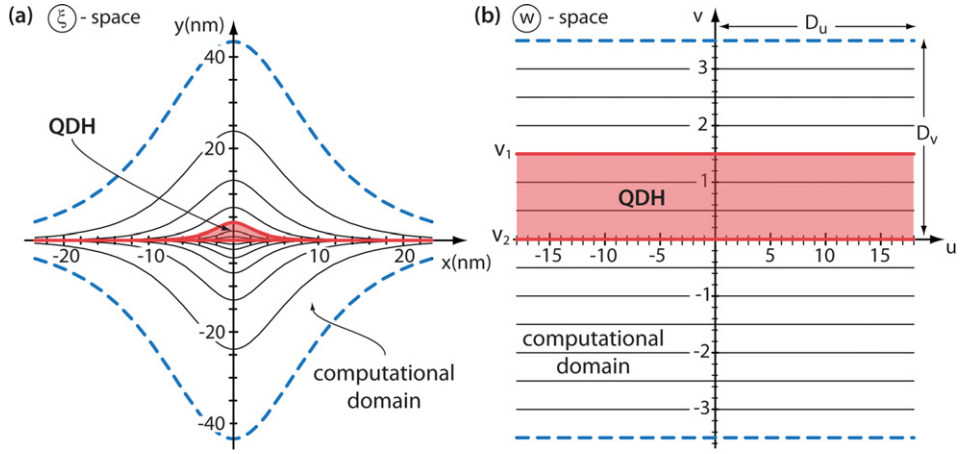

Fig. 4. (Color online.) The cross-section profile of QDH and the computational domain in the (a) ξ- and (b) w-space.

$$y_v = \frac{\partial y}{\partial v} = C\frac{A\cosh(Av) + BKu\sinh(Av)\sinh(Kv)\frac{\tanh[Bu/\cosh(Kv)]}{\cosh^2(Kv)}}{\cosh[Bu/\cosh(Kv)]}. \tag{10}$$

The functions which determine the elements in the Jacobian matrices J_{uv} and J_{xy} are given in Appendix A. Relation (10) determines $|J_{uv}|/C$, which is different from zero for any argument u and v, providing the existence of the inverse coordinate transformation and J_{xy} matrix. Although $|J_{uv}|$ has no zeros within the computational domain, the determinant decreases with $|u|$ and approaches the zero for large $|u|$ and small $|v|$ and may affect the accuracy of computation. However, this situation does not occur in the practice for common sizes of the computational domain. From the previous discussion, we conclude that the chosen transformation satisfies the most important requirements for successful implementation of the FDM including a significant domain enlargement for small variation in v.

As it is already mentioned, the profile of the QDH cross-section in some cases can be approximated with a trapezoidal shape, which can be fitted by the proper combination of the functions enlisted in Table 1. One possible solution is to use the following coordinate transformation:

$$x = Cu, \tag{11a}$$

$$y = \frac{C\sinh(Av)}{\cosh[Bu^2/(F + Kv^2)]}. \tag{11b}$$

Although this mapping leads to the trapezoidal cross-section profile, in the case of very wide structures (large $|u|$), the Jacobian determinant is too small (≈ 0) and the mapping becomes inefficient. Thus, for such structures we adopt a modified mapping, for which the argument in denominator saturates for large $|u|$. In order to fit experimentally found trapezoidal cross-section profile given in [10], we use following coordinate transformation:

$$x = Cu, \tag{12a}$$

$$y = \frac{C\sinh(Av)}{\cosh[G\tanh(Bu^q)/\cosh(Kv^p)]}, \tag{12b}$$

where p and q are positive integers. The corresponding elements of the Jacobian matrices J_{uv} and J_{xy} for the coordinate transformation given by relation (12) are given in Appendix B. The conclusions concerning the coordinate transformation features derived for the lens-like approximation are also valid in this case.

4. Computational results and discussion

In order to characterize and explore our method, we analyze the influence of the grid density and the computational domain size on the calculated eigenenergies. The first step in this analysis is to find a computational domain, for which the wavefunctions, corresponding to the eigenenergies of the QDH, can completely accommodate in the domain. The dimensions of the QDH given in Fig. 4 ($W \approx 14$ nm, $H = 3.5$ nm) are typical for InAs/GaAs material system. For this QDH structure, we find two bound states in the conduction band. As shown in Fig. 4(b), the upper heterointerface is mapped into $v_1 = 1.5$, while the lower corresponds to $v_2 = 0$. The selected domain size in the mapped space is $D_u = \pm 17$ and $D_v = \pm 3.5$, while the fitting parameters are $C = 1.3$ nm, $A = 1.2$, $B = 1$, $K = 0.7$.

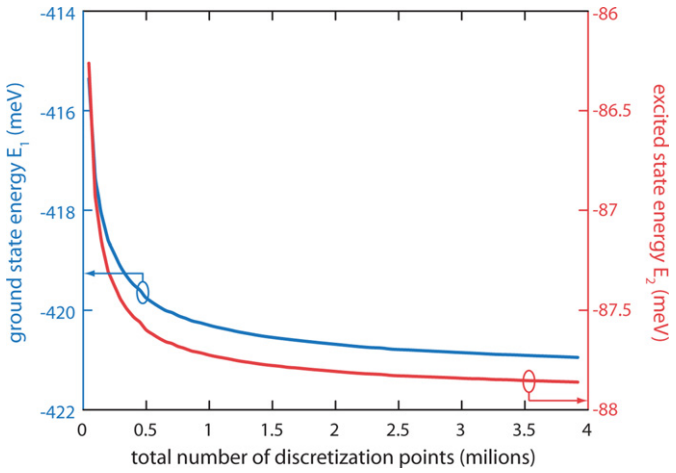

Fig. 5. (Color online.) The ground and the 1st excited state energy versus the total number of discretization points.

For the selected domain, we proportionally and gradually change the grid density in both directions and calculate eigenvalues for the QDH in Fig. 4. The discretization steps are equal in both directions, i.e. $\Delta = h_u = h_v$. Since the domain is fixed and the discretization steps are same in both directions, mutual ratio of the number of points in both directions is kept fixed. Thus, in further consideration, we do not consider the number of points in each direction (N_u, N_v), but rather the total number of grid points $(N_{uv} = N_u \times N_v)$, corresponding to the size of the discretization matrix. We use this quantity as a figure of merit for the computational time and memory resources required by the method.

Fig. 5 shows dependence of the calculated eigenenergies for both bound states versus the total number of grid points N_{uv}. It can be seen that for small number of the grid points, the eigenenergies rapidly decay and then gradually saturate with further increase in the grid density. The threshold of saturation is not clearly noticeable, although it can be seen that the difference between the eigenvalues for the largest $(\approx 4 \cdot 10^6)$ and any other grid density, becomes smaller than 1 meV, when the total number of grid points is larger than $6 \cdot 10^5$, for the ground state, and $3 \cdot 10^5$, for the

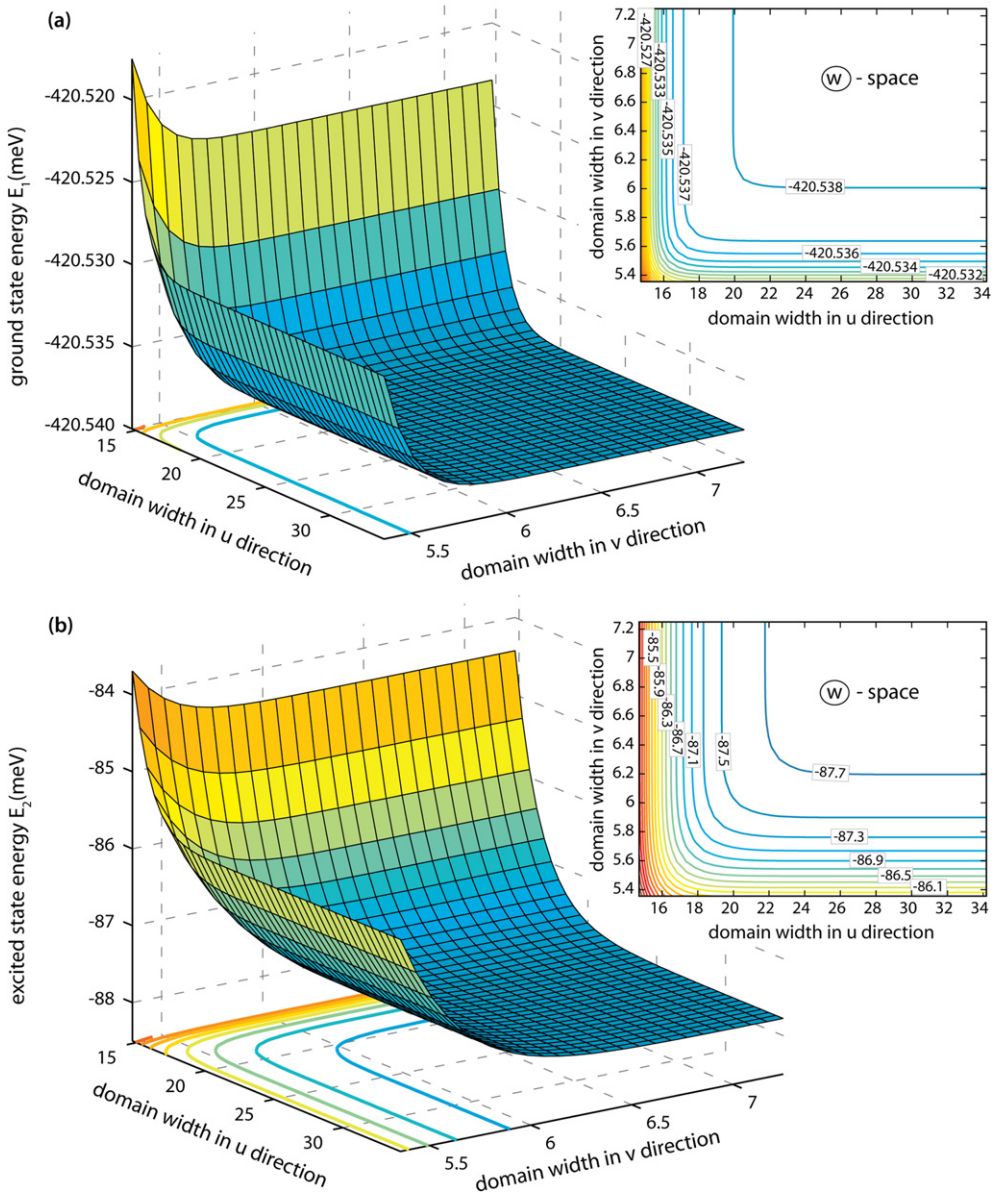

Fig. 6. (Color online.) Energy of the ground (a) and the 1st excited state (b) versus computational domain size in the w-space.

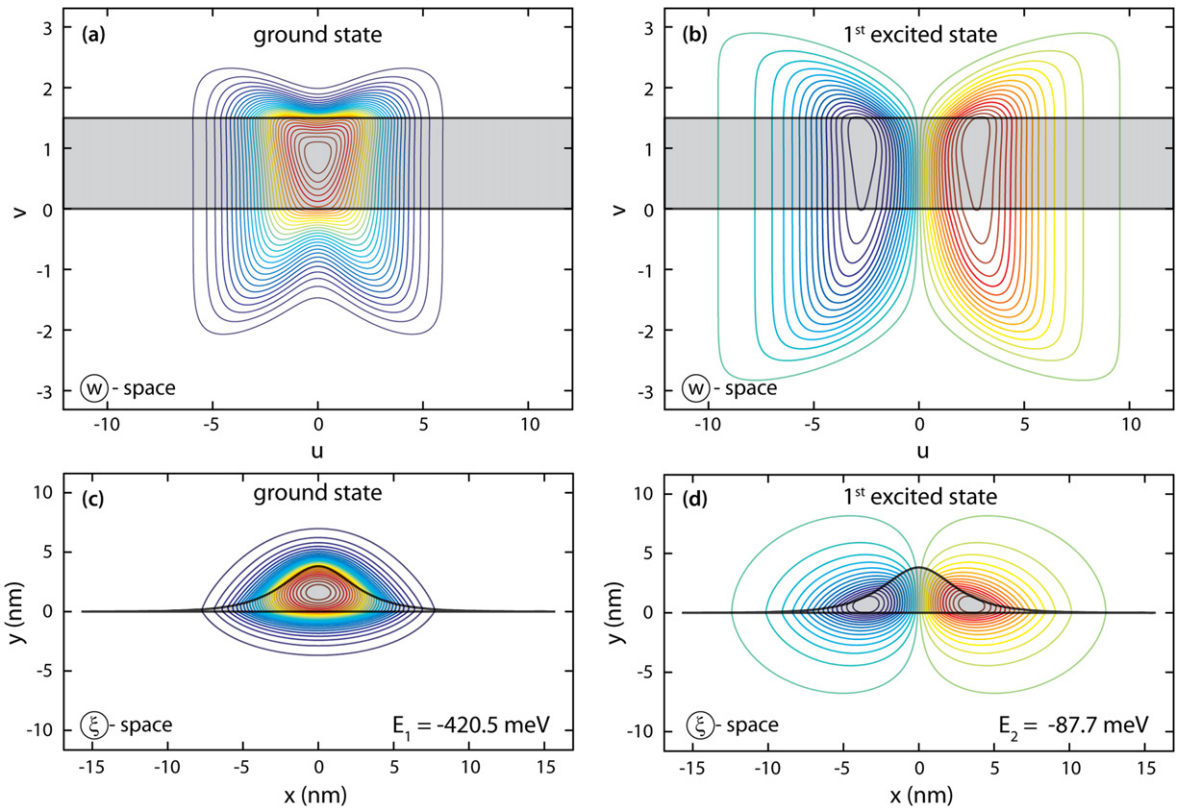

Fig. 7. (Color online.) Contour plot of the wavefunctions for the ground and 1st excited state in the ξ- and w-space for the QDH structure given in Fig. 4.

1st excited state. It means that the 1st excited state is less sensitive on the grid density than the ground state. Moreover, the total variation in the energy of the 1st excited state (from -86.3 meV to -87.8 meV) with the number of discretization points is almost four times smaller than for the ground state (from -415 meV to -421.2 meV). In order to achieve a trade-off between the accuracy and the computational time, we set a criterion for the optimal number of grid points. If the deviation of calculated eigenenergies from the eigenenergy obtained for the largest number of discretization points is smaller than 1 meV, for all eigenstates, we consider the number of discretization points sufficient and acceptable for further computation. According to Fig. 5 we find that the minimum number of total discretization points for the given computational domain and accurate calculation is $6 \cdot 10^5$. In other words, this number of points is the optimal one, for the adopted domain size and accuracy of 1 meV.

By using the dependence shown in Fig. 5, we are able to calculate the convergence rate of our method, which is ≈ 1 for the ground state and ≈ 1.3 for the first excited state [25]. This is an expected result, having in mind that the standard version of the finite differences has been implemented. However, the convergence rate can be improved by implementation of more sophisticated discretization methods, which we do not study here.

In order to make a fair comparison with the FEM, we perform the FEM calculation on the computational domain in ξ-space, which fully corresponds to domain used by our method in w-space. At the same time, we keep the number of elements in the FEM computation approximately equal to the number of points N_{uv}. However, a direct correspondence between number of points in our methods and elements in the FEM is not fully justified since the mesh in the FEM is not homogeneous as in the FDM. We find a fairly good agreement with our calculation, for which the eigenenergies differ less than one tenth of 1 meV from the eigenenergies calculated by the FEM. Regarding the computational time, we find our method more favorable than the FEM. As an illustration, we present the test of two methods performed on a desktop computer using 64-bit Windows 7 platform with Intel Core2Quad@2.66 GHz processor and 8 GB DDR2 memory (available physical memory 6.47 GB). After setting the number of discretization points (or FEM elements) to $N_{uv} = 0.55$, 1.27, 1.87 millions, our method completes calculation in 2.3, 13, and 34.1 min, while the FEM runs for 15.5, 82.3, and 179.6 min, respectively. This indicates that our method is at least 5 times faster than the FEM. Although our method is still superior for larger number of points, the comparison is not further reliable since both methods start to use virtual memory.

In Fig. 6 we show the energies of the ground and the first excited state versus the domain size in the u and v direction, for a fixed discretization step $\Delta = 0.013$. As one may expect, if the domain size is too small either in the u or v direction, the wavefunction cannot accommodate properly in the computational domain. In this case, a narrow domain acts as an additional infinite potential, raising the eigenenergies of both bound states. The domain for which the energy of the excited state reaches the saturation is not easy to recognize, although one can roughly adopt the region $2D_u \geqslant 20$ and $2D_v \geqslant 5.8$, for which variation in the eigenenergy is smaller than 0.5 meV. The situation is much more favorable for the ground state, which is less sensitive on variations in the domain size. In this case, the order of magnitude of the ground state energy variation is 10^{-2} meV for all considered dimensions of the computational domain, which is almost negligible in comparison with the first excited state. It can be seen that the saturation region is much more pronounced than for the excited state and comprises region $2D_u \geqslant 18$ and $2D_v \geqslant 5.7$, in which the energy variation is smaller than 10^{-3} meV. It should be noted that the sufficient domain size in w-space does not depend on actual QDH size but rather on its shape i.e. its width and height ratio. This feature is enabled by scaling factor C, which is used to set all

dashes of the same shape, regardless to their size, into the same domain in w-space.

In Fig. 7 we show the distribution of the wavefunction in the $\xi = \xi(x, y)$ and $w = w(u, v)$ space. It can be seen that in the w-space the wavefunctions for both states (Fig. 7(a)) are compressed along the v-direction in the middle of the computational domain. This is a consequence of implemented mapping, which in the w-space expands the region in the vicinity of the QDH corners and simultaneously compresses the space in the middle of the QDH. After implementation of the inverse mapping from the w- to the ξ-space, both wavefunctions nicely fit in the chosen computational domain.

In the case of trapezoidal QDH given in Ref. [10], we use the coordinate transformation (12) and find following fitting parameters: $p = 2$, $q = 6$, $A = 1$, $C = 1.5$ nm, $G = 20$, $B = 10^{-5}$, and $K = 1$. The corresponding fit of the QDH cross-section profile and the computational domain in the ξ-space are shown in Fig. 8. The form of the computational domain in the mapped space is the same as in Fig. 4(b). It should be noted that the mapping given by relations (11), although simpler, can reproduce narrower and higher trapezoidal shapes.

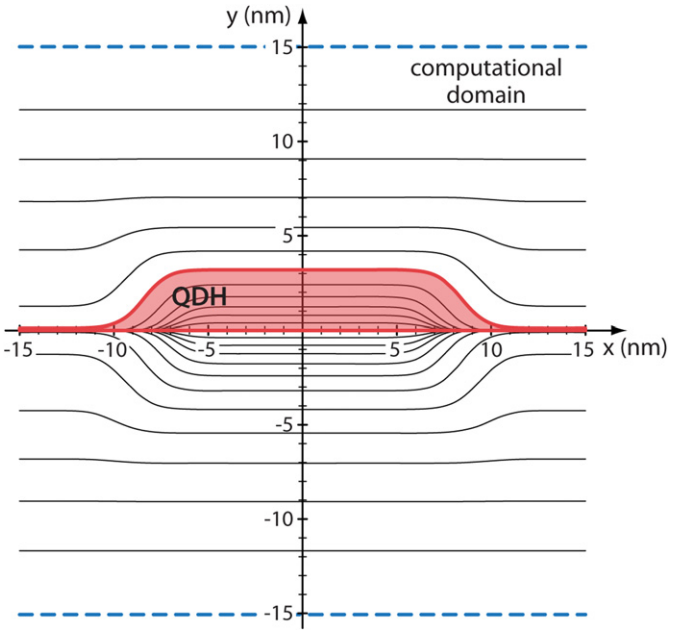

Fig. 8. (Color online.) The trapezoidal QDH profile and corresponding computational domain.

By implementing the same procedure as before, we calculate the corresponding discrete energies and wavefunctions shown in Fig. 9, which nicely accommodate into the selected computational domain. However, the problem in this case is the elongated shape of the QDH profile, which in comparison with the height of the QDH is one order of the magnitude larger and thus very difficult to fit with a simple combination of functions. Relation (12) provides not only a very broad and flat upper heterointerface of the QDH, but also the proper angle of the lateral sides of the trapeze. This angle is very important since it significantly affects the wavefunction distribution and indicates that approximation of the QDH by simple rectangular shape is not an adequate replacement for the trapezoidal profile. Moreover, the proposed coordinate transformation and the method simplify the implementation of the FDM, compared to the case when the problem is solved in the original ξ-space.

5. Conclusion

The paper presents an efficient and simple method for the band structure and wavefunction calculation of quantum dashes. The method is based on the coordinate transformation of the QDH structure, the computational domain and the Hamiltonian, followed by implementation of the FDM in the new computational space. The method versatility comes from a broad set of function families which can fit the upper QDH heterointerface and generate the computational domain of the proper form and size. Some of these functions are proposed in the paper and their features are studied. We find that the coordinate transformation (9) provides simple and flexible fitting of the most common, lens-like QDH profile, while the transformation (12) is very suitable for trapezoidal QDH cross-section shape. Our numerical investigation showed that there is a sufficient computational domain size, for which the variation of the eigenenergies with domain size can be reduced below a certain limit, in our case 10^{-2} meV. For the considered lens-like profile, the sufficient domain size is $2D_u \geqslant 20$ and $2D_v \geqslant 5.8$. The limits of the sufficient domain, and consequently the total

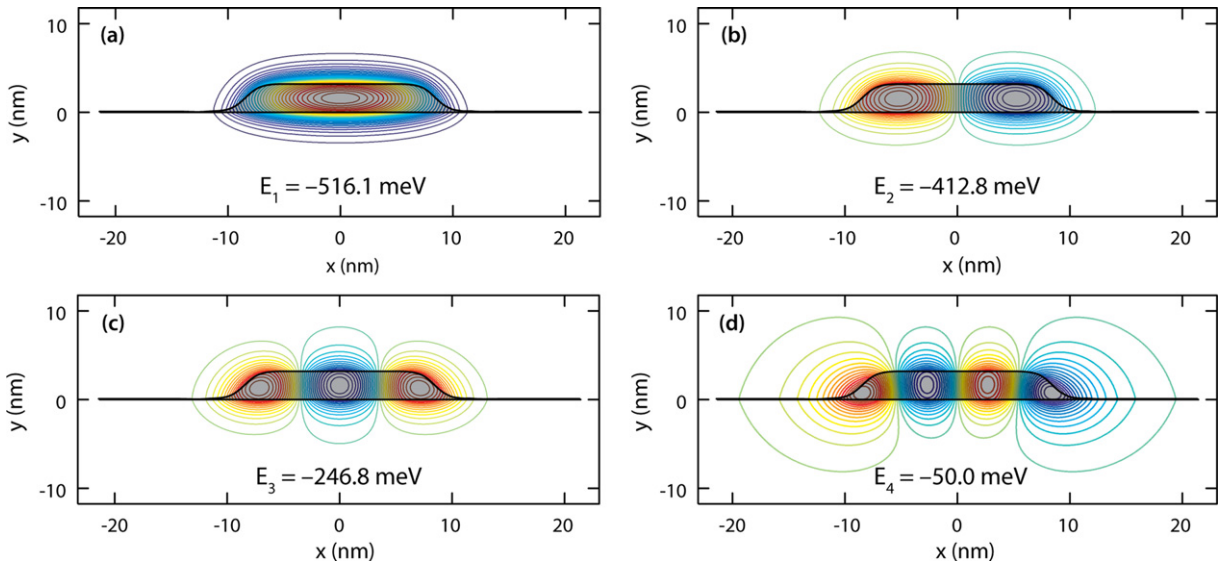

Fig. 9. (Color online.) Contour plot of the wavefunctions for the ground (a) and the first three excited states (b–d) in the ξ-space for the trapezoidal QDH structure in Fig. 8.

number of discretization points, do not depend on QDH size, but rather on their shape and dimensions ratio. Thus, the domain is the universal domain for QDHs with same shape and different sizes. For given QDH lens-like profile and the optimal total number of points (approximately $6 \cdot 10^5$) or even larger, the method provides stable eigenvalue solutions. The proposed method exhibits solid stability and flexibility with respect to the size and shape of the QDH and the computational domain. Due to its simplicity, it is very promising for implementation in the case of multiband Schrödinger-equation.

Acknowledgement

This work is supported by the Serbian Ministry of Science under project No. 160001.

Appendix A. The elements in the Jacobian matrices J_{uv} and J_{xy} for QDHs with the lens-like cross-section profile

For the coordinate transformation given by Eq. (9), the elements of the Jacobian matrix J_{uv} are:

$$y_u = \frac{\partial y}{\partial u} = -C\frac{B\sinh(Av)\sinh\left[\frac{Bu}{\cosh(Kv)}\right]}{\cosh(Kv)\cosh^2\left[\frac{Bu}{\cosh(Kv)}\right]}, \tag{A.1}$$

$$y_v = \frac{\partial y}{\partial v} = C\frac{A\cosh(Av) + BKu\sinh(Av)\frac{\sinh(Kv)}{\cosh^2(Kv)}\tanh\left[\frac{Bu}{\cosh(Kv)}\right]}{\cosh\left[\frac{Bu}{\cosh(Kv)}\right]}, \tag{A.2}$$

while, the elements of Jacobian matrix J_{xy} are:

$$v_x = \frac{\partial v}{\partial x} = \frac{1}{C}\frac{B\frac{\sinh(Av)}{\cosh(Kv)}\tanh\left[\frac{Bu}{\cosh(Kv)}\right]}{A\cosh(Av) + BKu\sinh(Av)\frac{\sinh(Kv)}{\cosh^2(Kv)}\tanh\left[\frac{Bu}{\cosh(Kv)}\right]}, \tag{A.3}$$

$$v_y = \frac{\partial v}{\partial y} = \frac{1}{C}\frac{\cosh\left[\frac{Bu}{\cosh(Kv)}\right]}{A\cosh(Av) + BKu\sinh(Av)\cdot\frac{\sinh(Kv)}{\cosh^2(Kv)}\tanh\left[\frac{Bu}{\cosh(Kv)}\right]}. \tag{A.4}$$

Appendix B. The elements in the Jacobian matrices J_{uv} and J_{xy} for QDHs with the trapezoidal cross-section profile

For the coordinate transformation given by Eq. (12), the elements of the Jacobian matrix J_{uv} are:

$$y_u = \frac{\partial y}{\partial u} = \frac{-CBGqu^{q-1}\sinh(Av)\tanh\left[G\frac{\tanh(Bu^q)}{\cosh(Kv^p)}\right]}{\cosh^2(Bu^q)\cosh(Kv^p)\cosh\left[G\frac{\tanh(Bu^q)}{\cosh(Kv^p)}\right]}, \tag{B.1}$$

$$y_v = \frac{\partial y}{\partial v} = C\left(A\cosh(Av) + KGpv^{p-1}\sinh(Av) \times \tanh(Bu^q)\frac{\tanh(Kv^p)}{\cosh(Kv^p)}\tanh\left[G\frac{\tanh(Bu^q)}{\cosh(Kv^p)}\right]\right) \times \left(\cosh\left[G\frac{\tanh(Bu^q)}{\cosh(Kv^p)}\right]\right)^{-1}, \tag{B.2}$$

while the elements of the Jacobian matrix J_{xy} are:

$$v_x = \frac{\partial v}{\partial x} = \frac{BGqu^{q-1}\sinh(Av)\tanh\left[G\frac{\tanh(Bu^q)}{\cosh(Kv^p)}\right]}{C\cosh^2(Bu^q)\cosh(Kv^p)} \times \left\{A\cosh(Av) + GKpv^{p-1}\sinh(Av) \times \tanh(Bu^q)\frac{\tanh(Kv^p)}{\cosh(Kv^p)}\tanh\left[G\frac{\tanh(Bu^q)}{\cosh(Kv^p)}\right]\right\}^{-1}, \tag{B.3}$$

$$v_y = \frac{\partial v}{\partial y} = \left(\frac{1}{C}\cosh\left[G\frac{\tanh(Bu^q)}{\cosh(Kv^p)}\right]\right) \times \left(A\cosh(Av) + GKpv^{p-1}\sinh(Av) \times \tanh(Bu^q)\frac{\tanh(Kv^p)}{\cosh(Kv^p)}\tanh\left[G\frac{\tanh(Bu^q)}{\cosh(Kv^p)}\right]\right)^{-1}. \tag{B.4}$$

References

[1] P. Bhattacharya, Z. Mi, Quantum-dot optoelectronic devices, Proc. IEEE 95 (2007) 1723–1740.
[2] J.P. Reithmaier, G. Eisenstein, A. Forchel, InAs/InP quantum-dash lasers and amplifiers, Proc. IEEE 95 (2007) 1779–1790.
[3] F. Lelarge, B. Dagens, J. Renaudier, R. Brenot, A. Accard, F. van Dijk, D. Make, O. Le Gouezigou, J.-G. Provost, F. Poingt, J. Landreau, O. Drisse, E. Derouin, B. Rousseau, F. Pommereau, G.-H. Duan, Recent advances on InAs/InP quantum dash based semiconductor lasers and optical amplifiers operating at 1.55 μm, IEEE J. Sel. Top. Quantum Electron. 13 (2007) 111–124.
[4] J.P. Reithmaier, A. Somers, S. Deubert, R. Schwertberger, W. Kaiser, A. Forchel, M. Calligaro, P. Resneau, O. Parillaud, S. Bansropun, M. Krakowski, R. Alizon, D. Hadass, A. Bilenca, H. Dery, V. Mikhelashvili, G. Eisenstein, M. Gioannini, I. Montrosset, T.W. Berg, M. van der Poel, J. Mørk, B. Tromborg, InP based lasers and optical amplifiers with wire-/dot-like active regions, J. Phys. D: Appl. Phys. 38 (2005) 2088–2102.
[5] A.J. Zilkie, J. Meier, M. Mojahedi, P.J. Poole, P. Barrios, D. Poitras, T.J. Rotter, C. Yang, A. Stintz, K.J. Malloy, P.W.E. Smith, J.S. Aitchison, Carrier dynamics of quantum-dot, quantum-dash, and quantum-well semiconductor optical amplifiers operating at 1.55 μm, IEEE J. Quantum Electron. 43 (2007) 982–991.
[6] A. Stintz, G.T. Liu, H. Li, L.F. Lester, K.J. Malloy, Low-threshold current density 1.3-μm InAs quantum-dot lasers with the dots-in-a-well (DWELL) structure, IEEE Photon. Technol. Lett. 12 (2000) 591–593.
[7] H. Saito, K. Nishi, A. Kamei, S. Sugou, Low chirp observed in directly modulated quantum dot lasers, IEEE Photon. Technol. Lett. 12 (2000) 1298–1300.
[8] J.H. Wei, K.S. Chan, A theoretical analysis of quantum dash structures, J. Appl. Phys. 97 (2005) 123524–123539.
[9] H. Dery, E. Benisty, A. Epstein, R. Alizon, V. Mikhelashvili, G. Eisenstein, R. Schwertberger, D. Gold, J.P. Reithmaier, A. Forchel, On the nature of quantum dash structures, J. Appl. Phys. 95 (2004) 6103–6111.
[10] H.S. Djie, C.L. Tan, B.S. Ooi, J.C.M. Hwang, X.-M. Fang, Y. Wu, J.M. Fastenau, W.K. Liu, G.T. Dang, W.H. Chang, Ultrabroad stimulated emission from quantum-dash laser, Appl. Phys. Lett. 91 (2007) 111116–111119.
[11] J.V. Crnjanski, D.M. Gvozdić, Intersubband absorption in quantum dash nanostructures, Acta Phys. Pol. A 116 (2009) 668–671.
[12] M. Gioannini, Analysis of the optical gain characteristics of semiconductor quantum-dash materials including the band structure modifications due to the wetting layer, IEEE J. Quantum Electron. 42 (2006) 331–340.
[13] T. Yamauchi, T. Takahashi, Y. Arakawa, Tight binding analysis for quantum-wire lasers and quantum-wire infrared detectors, IEEE J. Quantum Electron. 27 (1991) 1817–1823.
[14] S. Pescetelli, A.D. Carlo, P. Lugli, Conduction-band mixing in T and V-shaped quantum wires, Phys. Rev. B 56 (1997) R1668–R1671.
[15] F. Vouilloz, D.Y. Oberli, M.-A. Dupertuis, A. Gustafsson, F. Reinhardt, E. Kapon, Effect of lateral confinement on valence-band mixing and polarization anisotropy in quantum wires, Phys. Rev. B 57 (1998) 12378–12387.
[16] J.C. Yi, N. Dagli, Finite-element analysis of valence band structure and optical properties of quantum-wire arrays on vicinal substrates, IEEE J. Quantum Electron. 31 (1995) 208–218.
[17] M. Ogawa, T. Kunimasa, T. Ito, T. Miyoshi, Finite-element analysis of quantum wires with arbitrary cross sections, J. Appl. Phys. 84 (1998) 3242–3249.
[18] D.M. Gvozdić, N.M. Nenadović, A. Schlachetzki, Gain and threshold-current calculation of V-groove quantum-wire InGaAs–InP laser, IEEE J. Quantum Electron. 38 (2002) 1565–1579.
[19] D.M. Gvozdić, A. Schlachetzki, Electronic states in the conduction band of V-groove quantum wires, J. Appl. Phys. 92 (2002) 2023–2034.

[20] G. Goldoni, F. Rossi, E. Molinari, A. Fasolino, Band structure and optical anisotropy in V-shaped and T-shaped semiconductor quantum wires, Phys. Rev. B 55 (1997) 7110–7123.
[21] U. Ekenberg, D.M. Gvozdić, Analysis of electric-field-induced spin splitting in wide modulation-doped quantum wells, Phys. Rev. B 78 (2008) 205317–205326.
[22] C. Pryor, Electronic structure and optical properties of serpentine superlattice quantum-wire arrays, Phys. Rev. B 44 (1991) 12912–12917.
[23] T.-M. Hwang, W.-W. Lin, W.-C. Wang, W. Wang, Numerical simulation of three dimensional pyramid quantum dot, J. Comput. Phys. 196 (2004) 208–232.
[24] C.J. Fall, M.-A. Dupertuis, E. Kapon, Electronic states in hyperbolic-boundary crescent-shaped quantum wires, Opt. Quantum Electron. 31 (1999) 201–213.
[25] T.-M. Hwang, W.-C. Wang, W. Wang, Numerical schemes for three-dimensional irregular shape quantum dots over curvilinear coordinate systems, J. Comput. Phys. 226 (2007) 754–773.
[26] G. Creci, G. Weber, Electron and hole states in V-groove quantum wires: an effective potential calculation, Semicond. Sci. Technol. 14 (1999) 690–694.
[27] W. Rudno-Rudziński, G. Sęk, K. Ryczko, R. Kudrawiec, J. Misiewicz, A. Somers, R. Schwertberger, J.P. Reithmaier, A. Forchel, Optically probed wetting layer in InAs/InGaAlAs/InP quantum-dash structures, Appl. Phys. Lett. 86 (2005) 101904–101906.
[28] B.S. Ooi, H.S. Dije, Y. Wang, C.-L. Tan, J.C.M. Hwang, X.-M. Fang, J.M. Fastenau, A.W.K. Liu, G.T. Dang, W.H. Chang, Quantum dashes on InP supstrate for broadband emitter applications, IEEE J. Sel. Top. Quantum Electron. 14 (2008) 1230–1238.
[29] P. Miska, J. Even, C. Platz, B. Salem, T. Benyattou, C. Bru-Chevalier, G. Guillot, G. Bremond, Kh. Moumanis, F.H. Julien, O. Marty, C. Monat, M. Gendry, Experimental and theoretical investigation of carrier confinement in InAs quantum dashes grown on InP(001), J. Appl. Phys. 95 (2004) 1074–1080.
[30] I. Vurgaftman, J.R. Meyer, L.R. Ram-Mohan, Band parameters for III–V compound semiconductors and their alloys, J. Appl. Phys. 89 (2001) 5815–5875.
[31] S.P. Guo, H. Ohno, A. Shen, F. Matsukura, Y. Ohno, InAs self-organised quantum dashes grown on GaAs (211)B, Appl. Phys. Lett. 70 (1997) 2738–2740.
[32] A. Sauerwald, T. Kümmell, G. Bacher, A. Somers, R. Schwertberger, J.P. Reithmaier, A. Forchel, Size control of InAs quantum dashes, Appl. Phys. Lett. 86 (2005) 253112–253114.
[33] S.C. Heck, S.B. Healy, S. Osborne, E.P. O'Reilly, F. Lelarge, F. Poingt, A. Accard, F. Pommereau, O. Le Gouezigou, B. Dagens, An analysis of 1.55 μm InAs/InP quantum dash lasers, Appl. Phys. Lett. 92 (2008) 251105–251107.
[34] Z. Mi, P. Bhattacharya, DC and dynamic characteristics of P-doped and tunnel injection 1.65-μm InAs quantum-dash lasers grown on InP (001), IEEE J. Quantum Electron. 42 (2006) 1224–1232.

RESEARCH ARTICLE | DECEMBER 21 2012

Miniband electronic structure of quantum dash array

B. M. Stupovski; J. V. Crnjanski; D. M. Gvozdić

Journal of Applied Physics 112, 123716 (2012)
https://doi.org/10.1063/1.4770437

Miniband electronic structure of quantum dash array

B. M. Stupovski, J. V. Crnjanski, and D. M. Gvozdić
Faculty of Electrical Engineering, University of Belgrade, Bulevar Kralja Aleksandra 73b, P.O. Box 35-54, 11120 Belgrade, Serbia

(Received 17 October 2012; accepted 19 November 2012; published online 21 December 2012)

In the paper, we investigate the miniband structure of one-dimensional quantum dash array and its dependence on geometrical parameters by using a newly developed and efficient numerical method. We show that miniband energy significantly depends on the dash height and width, while the miniband width depends on the array period and the dash width. The excited minibands may exhibit the effect of zero miniband gap and the multiple anticrossings, which are followed by the swapping of the character of adjacent minibands top and bottom. The wetting layer allows formation of a miniband cluster in the vicinity of the well top, which essentially represents the barrier continuum embedded into the well of array. © *2012 American Institute of Physics*. [http://dx.doi.org/10.1063/1.4770437]

I. INTRODUCTION

Recent studies have shown that photonic devices incorporating semiconductor nanostructures in which the electronic motion is confined in more than one spatial direction, may overcome some of the limitations of quantum well based devices, especially short excited-state carrier lifetime,[1] caused by numerous in-plane scattering paths.[2] Self-assembled nanostructures, as three-dimensionally (3D) confined quantum dots (QDs) or their elongated version with 2D confinement, called quantum dashes (QDH), may provide the additional confinement required for reduction of scattering events or improvement of optical transitions strength and polarization. Therefore, investigation of their electronic structure is a basis for further understanding and optimization with respect to carrier scattering processes and its lifetime, optical transitions strength and polarization type.

The electronic band structure in these nanostructures is usually studied thoroughly for an isolated system comprising the well and the barrier region and corresponding strain and potential distribution.[3–8] However, due to self-assembled growth, these nanostructures form an ensemble in which dots or dashes are usually distributed in the close proximity of each other, leading to a quantum mechanical coupling.[9] Due to the coupling, the electronic band structure as well as the optical properties of these nanostructures may significantly differ from those for an isolated dot or dash.

In this paper, we present an efficient numerical method, based on coordinate transformation and the finite differences method, which provides calculation of electronic band structure of quantum dash array. In the case of sufficiently high compressive strain, which is common for QDHs, it is possible to consider heavy and light holes decoupled and apply this method even in the calculation of the QDH valence band structure.[5,9] Due to a stochastic distribution, QDH array may consist of dashes with different cross-section, which means that their width, height, shape and even separation of adjacent dashes might be different.[8–11] However, our model is based on the assumption that the QDH ensemble consists of equally long dashes with the same cross-section profile distributed in a periodic array. Although the model can not provide precise insight into electronic band structure of array consisting of QDHs with randomized cross-section dimensions, it can help to understand and reveal the influence of different geometrical parameters of the QDH array on the electronic band structure. Therefore, we investigate how the QDH width and height as well as the period of array, affect electronic states in the QDH conduction band.

We focus our investigation on two different material systems. As first, we study InAs/InAlGaAs QDHs, where InAlGaAs is latticed matched to InP. Although this material system is useful for telecom applications due to interband emission at 1.5 μm, it was recently implemented as the active region of a quantum cascade laser.[2] However, the well in this material system is shallow and doesn't provide sufficient depth for different minibands and effects which may occur in deeper wells. Thus, we extend our research on InAs/GaAs QDHs, which due to a larger depth exhibit more interesting effects in the electronic band structure.

In Sec. II, we give details of our method, which combines specially designed coordinate mappings and finite differences for calculation of electronic band structure. In Sec. III, we present application of the method to InAs/InAlGaAs QDH array. In this section, we show and discuss how electronic minibands depend on the QDH height, full width at half of the height, and the array period, and compare results obtained for different material systems. In the last section we present conclusions of this paper.

II. DESCRIPTION OF THE METHOD

In our analysis of minibands, we take into account the wetting layer (WL), formed as a consequence of self-assembled growth of InAs islands. The strength of quantum mechanical coupling between dashes in the QDH material depends on the WL thickness (t_W) and the density of QDHs, as well as on the actual profile of the QDH's cross-section. The WL thickness t_W is defined as the well material thickness in the middle of two neighbouring QDHs [Fig. 1(a)]. Parameters of the QDH cross section are the maximum

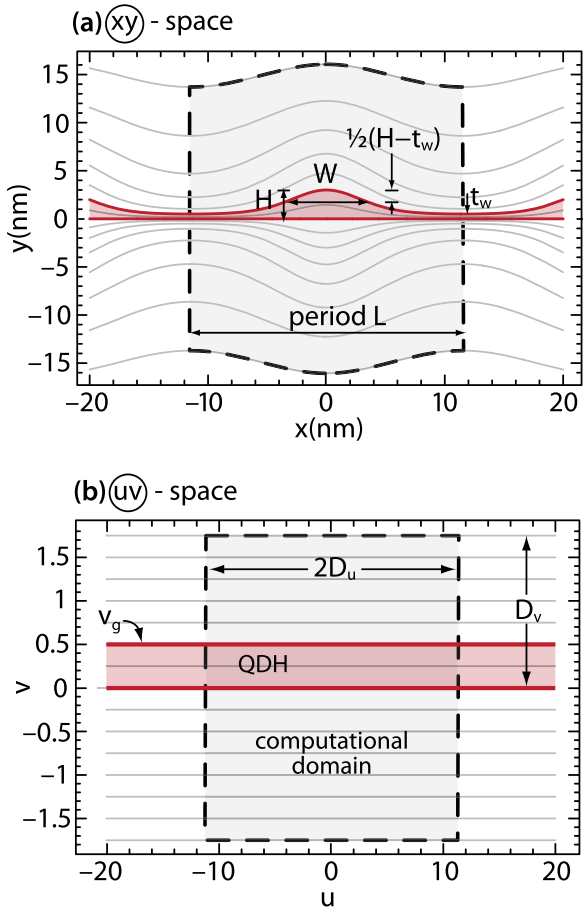

FIG. 1. The cross-section profile of QDH array and the computational domain in (a) the real xy-space, and in (b) the mapped uv-space. Dashed lines represent boundaries of the computational domain and the elementary cell of the QDH array.

height of the QDH array denoted by H, and the full width at half maximum W of a single QDH with respect to the wetting layer thickness [Fig. 1(a)]. Material parameters and the conduction band offset (Table I) are taken from Refs. 12 and 13, assuming compressively strained dashes.[9] Since QDHs exhibit the quantum-wire like nature,[4] we approximate them with infinitely long wires and focus only on their profile of carrier confinement in the transversal x-y plane [Fig. 1(a)]. Thus, the quantization in the longitudinal z-direction leads to a quasi-continuous subband structure, the energy of which is well approximated with parabolic dependence on corresponding wave vector k_z.

The conduction band structure of the periodic array of QDHs is modelled by using the single-band Schrödinger equation in the envelope function approximation:

$$-\frac{\hbar^2}{2}\left[\frac{\partial}{\partial x}\left(\frac{1}{m^*}\frac{\partial\psi}{\partial x}\right)+\frac{\partial}{\partial y}\left(\frac{1}{m^*}\frac{\partial\psi}{\partial y}\right)\right]+\left[\frac{\hbar^2 k_z^2}{2m^*}+U\right]\psi=E\psi, \tag{1}$$

TABLE I. Material parameters used for band calculation.

	InAs	GaAs	$In_{0.53}Ga_{0.23}Al_{0.24}As$
$m^*(m_0)$	0.0221	0.0623	0.0547
ΔE_c(meV)		858.7	396.9

where $\psi=\psi(x,y)$ is slowly varying part of the total wavefunction, $U=U(x,\ y)$ is the 2D potential profile determined by the heterointerface of the well and the matrix material and the conduction band offset ΔE_c, $m^*=m^*(x,y)$ is the electronic effective mass, while E is the confinement energy referenced to the conduction band edge of the QDH barrier material. In our analysis, we are interested only in the eigenenergies corresponding to the subband bottom, for which $k_z=0$.

Although realistic QDH ensemble comprises nonuniformly distributed InAs islands, in our calculation we analyze the array of identical QDHs equally spaced in the x-direction. Therefore solution of Eq. (1) satisfies Bloch theorem for the wave function $\psi(x,y)$ in periodic potential:

$$\psi(x+L,y)=\exp(\imath KL)\psi(x,y), \tag{2}$$

where L is the period of QDH array in the x-direction, while K is Bloch wave number (miniband wavevector). The extreme values of the phase shift factor $\exp(\imath KL)$, $+1$ and -1, corresponding to $KL=0$ and $KL=\pi$, respectively, determine boundaries of the minibands and corresponding wavefunctions. Since the periodicity exists only in the x-direction, while in the y-direction there is no coupling between dashes, formation of the minibands is limited to the range of energies below the band edge of the QDH barrier material. The full periodicity can be achieved by stacking additional arrays of quantum dashes on the top of each other. In this case, the minibands can be formed in and above the well. In the paper, we focus on the single array of QDHs.

Depending on the material system, nominal thickness of the InAs layer and growth parameters, e.g. the growth temperature, group-III/V ratio and growth rate, self-assembled QDHs may have different dimensions and shapes of the cross-section profiles.[8–11] Thus, the functions used for coordinate transformation and the QDH cross-section profile fitting may differ significantly. Before we proceed with a detailed description of these functions, we generally present the method used for calculation of the electronic band structure.

The method is based on the combination of coordinate transformation and the finite differences method (FDM).[12] Essentially, the coordinate transformation maps the well, i.e., the profile of the dash array cross-section, and surrounding barrier space, which has to be sufficiently large to naturally accommodate the wavefunctions [Fig. 1(a)], into the computational domain with straight boundaries and heterointerfaces [Fig. 1(b)]. Since we apply the periodic boundary condition (2), the computational domain in the x-direction is limited to the elementary cell of the array, which is determined by the array period L. This converts the computational domain from infinite stripe into a rectangle, and enables the solving of the single-band Schrödinger equation in the new coordinates by straightforward implementation of the finite differences method.

The form of invertible coordinate transformation is given by:

$$\begin{aligned} x&=u;\\ y&=f(u,v). \end{aligned} \tag{3}$$

In order to describe the periodic array of QDHs and provide proper implementation of the boundary conditions, function $f(u, v)$ must be periodic with respect to u with period L. Moreover, suitable functions $f(u, v)$ should provide good fitting of the heterointerfaces in transversal plane, as well as rectangular profile of the well region within the elementary cell in the uv-space. Advantage of the approach based on coordinate mapping compared to direct implementation of FDM without the mapping is that potential problems with curvilinear boundary conditions or their careful implementation can be avoided.[14,15] Moreover, the profile of analyzed QDH can be varied simply by changing parameters of function $f(u, v)$.

By using coordinate transformations (3), Eq. (1) in the xy-space for $k_z = 0$ is mapped to equation:

$$-\frac{\hbar^2}{2}\left[\frac{\partial}{\partial u}\left(\frac{1}{m^*}\frac{\partial\psi}{\partial u}+\frac{\mu}{m^*}\frac{\partial\psi}{\partial v}\right)+\mu\frac{\partial}{\partial v}\left(\frac{1}{m^*}\frac{\partial\psi}{\partial u}+\frac{\mu}{m^*}\frac{\partial\psi}{\partial v}\right)+\rho\frac{\partial}{\partial v}\left(\frac{\rho}{m^*}\frac{\partial\psi}{\partial v}\right)\right]+U\psi=E\psi, \tag{4}$$

in the uv-space, where $\psi(u,v)=\psi[x(u,v),y(u,v)]$, $U(u,v)=U[x(u,v),y(u,v)]$, $m^*(u,v)=m^*[x(u,v),y(u,v)]$. According to the inverse function theorem, $\mu(u,v)$ and $\rho(u,v)$ are given by $\mu=\mu(u,v)=v_x=-f_u/f_v$, $\rho=\rho(u,v)=v_y=1/f_v$, where f_u and f_v denote partial derivatives of $f(u, v)$ with respect to u and v. Jacobian matrices J_{uv} and J_{xy} of transformation (3) and inverse transformation, respectively, are

$$J_{uv}=\begin{bmatrix}x_u & x_v\\ y_u & y_v\end{bmatrix}=\begin{bmatrix}1 & 0\\ f_u & f_v\end{bmatrix}, \tag{5a}$$

$$J_{xy}=\begin{bmatrix}u_x & u_y\\ v_x & v_y\end{bmatrix}=\begin{bmatrix}1 & 0\\ -f_u/f_v & 1/f_v\end{bmatrix}=\begin{bmatrix}1 & 0\\ \mu & \rho\end{bmatrix}, \tag{5b}$$

so that invertibility condition of transformation (3) is simply $|J_{uv}|=|J_{xy}|^{-1}=f_v\neq 0$. The form of transformation (3), as well as the periodicity of $f(u, v)$, provide that the periodic boundary condition (2) in the xy-space maps correctly into the uv-space and incorporates in the FDM scheme in straightforward manner. In case that $f(u, v)$ was an aperiodic function, the mapped space beyond the boundaries of the cell would be improperly mapped, which might lead to degradation of the boundary conditions.

The function $f(u, v)$, as well as $\mu(u,v)$ and $\rho(u,v)$, are given by analytical expressions. In addition, the well region corresponding to the elementary cell is a rectangle in the uv-space [Fig. 1(b)]. The computational domain in the uv-space is also a rectangle which is chosen to be large enough to comprise the well region of the elementary cell and corresponding wavefunctions [Fig. 1(b)]. Thus Eq. (4) can be directly discretized by using standard central differences.[12] Since the periodicity exists only in the u-direction, we apply Dirichlet boundary condition in the v-direction, i.e., $\psi(u,v)=0$ at the edge of the computational domain in the v-direction ($|v|=D_v$). The boundary condition in the u-direction is $\psi(L/2,v)=\exp(\imath KL)\psi(-L/2,v)$. The implementation of the finite differences scheme provides that the boundary conditions on heterointerfaces are naturally built in into the discretization and need not be enforced explicitly.

If the upper heterointerface of the QDH can be fitted by $y=f(u,v_g)=g(u)$, where v_g is corresponding v coordinate, all introduced parameters can be related to function $g(u)$ as follows: $t_W=g(\pm L/2)$, $H=g(0)$ and finally $(H-t_W)/2=g(\pm W/2)-t_W$, as shown in Fig. 1. Due to the symmetry of the profile of QDHs in the array, $f(u, v)$ and $g(u)$ are even functions with respect to u.

We first introduce transformation which provides fitting of the Gaussian-like QDH profile, given by following analytical expression (Gauss-mapping):

$$\begin{aligned}x&=u,\\ y&=f(u,v)\\ &=\sinh(Av)\left\{D+F\exp\left[-C\sin^2\left(\frac{\pi}{L}u\right)\exp(-Bv^2)\right]\right\}.\end{aligned} \tag{6}$$

As we already mentioned, the function $g(u)=f(u,v_g)$, fits the upper heterointerface of QDH in the xy-space for $v=v_g$, while the lower heterointerface of QDH, represented by the straight line $y=0$, corresponds to $v=0$. However, v_g is also a fitting parameter, which depends on the actual dimensions of the QDH elementary cell and positive constants A, B, C, D and F. Although all these parameters generally provide the fitting of the QDH cross-section profile and the adequate shape and dimensions of the computational domain, each of them differently affects the fitting of various geometrical parameters of the QDH elementary cell. For example, parameters A and B provide control of the computational domain dimensions in the xy-space. Once A and B are adopted, it is possible to investigate other parameters as C, D and F, which are relevant for precise fitting of the upper heterointerface within the elementary cell of QDH array. For example, D and F are used to fit the thickness of the wetting layer, since for common C and B-values the expression for the wetting layer thickness $t_W=g(\pm L/2)=\sinh(Av_g)\{D+F\exp[-C\exp(-Bv_g^2)]\}$, besides a scaling cofactor $\sinh(Av_g)$, is dominantly determined by D and F. In addition, D and F considerably affect the fit of the QDH height, since $g(0)=\sinh(Av_g)(D+F)$. Finally, C is used to fit the QDH width and its Gaussian-like profile. By using relation (6) it is possible to calculate C, D and F for a wide range of geometrical parameters t_W, H, W.

We find that coordinate transformation (6) cannot be used for fitting QDH arrays with densely packed QDHs. In this case, W/L ratio is relatively large, causing that C, D and F may not be positive. Moreover, the coordinate transformation becomes noninvertible. In order to analyze QDH arrays with large values of W/L, we use another coordinate transformation (Atanh-mapping) given by:

$$\begin{aligned}x&=u,\\ y&=f(u,v)=\frac{\sinh(Av)}{D+\operatorname{arctanh}[C\sin^2(\pi u/L)]/\cosh(Bv)}.\end{aligned} \tag{7}$$

Here, positive parameters v_g and B are used to control dimension of the computational domain in the xy-space. Once v_g and B are fixed, Eq. (7) can provide positive parameters A, C and D in terms of t_W, H, W.

Fig. 2(a) shows the profiles of QDHs, fitted by Atanh-mapping [Eq. (7)], for which the dash width W and the

period L are comparable. It can be seen that such QDH dimensions (i.e., $W = 7$ nm and $L = 8$ nm) correspond to almost vertical edges of the QDH elementary cells, which is common profile in the case of densely packed QDH arrays. The profile obtained from Atanh-mapping for relatively small ratios (e.g., $W = 7$ nm, $L = 20$ nm), can be equally well fitted by Gaussian profile defined by Eq. (6). For much smaller W/L ratios, the profile of QDH heterointerface can be better fitted by Gauss-mapping than by Atanh-mapping, since Eq. (6) provides very small values W/L. Figs. 2(b) and 2(c) show profiles of QDH array for various heights and all other parameters fixed, obtained for Atanh-mapping and Gauss-mapping, respectively. It can be seen that Eq. (6), which is used for larger L and smaller W/L ratio, provides broad range of Gaussian or lens-like QDH profiles with different heights [Fig. 2(c)], while Eq. (7), specialized for smaller L and larger W/L ratio, enables fitting of triangular-like profiles [Fig. 2(b)]. Figs. 2(d) and 2(e) depict the profile families derived from Eqs. (7) and (6), respectively, for which we vary the width W and keep all other parameters fixed. It can be seen that variation of W in the case of Gauss-mapping, besides lens-like profile, provides bell-like profile, for which the width can be very small. On the other hand, Atanh-mapping may produce much larger variety of profiles, which range from concave to convex shapes [Fig. 2(d)].

III. RESULTS AND DISCUSSION

The method described in Sec. II is generalization of the method we implemented on a single QDH.[12] Here, we extend the method to the one-dimensional array of QDHs, by using periodic functions for fitting the array heterointerface.

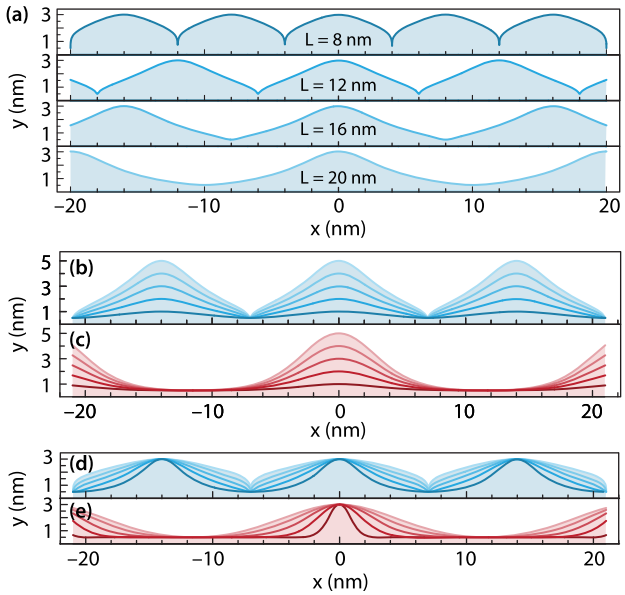

FIG. 2. Profile of the QDH cross-section (a) for $H = 3$ nm, $W = 7$ nm and various array periods $L = 8$, 12, 16, and 20 nm. Same for different heights $H = 1 - 5$ nm for QDH array with $W = 7$ nm and (b) $L = 14$ nm or (c) $L = 23$ nm. Same for different widths (d) $W = 4$, 6, 8, 10 and 12 nm for QDH array with $H = 3$ nm and $L = 14$ nm, and (e) $W = 2$, 4, 6, 8 and 10 nm for QDH array with $H = 3$ nm and $L = 23$ nm. Profiles in (a), (b), and (d) are obtained by fitting with Atanh-mapping, while (c) and (e) correspond to Gauss-mapping.

The efficiency and convergence of the method are already investigated and presented in the case of the single QDH.[12] Since the only significant change in the case of QDH array are fitting functions, which must satisfy the same conditions as those used for isolated QDHs, especially the invertibility condition described in the previous section, further investigation and characterization of the method are not needed. Essentially, the method proposed in Ref. 12 is revised to account for the periodic boundary conditions and instead of its implementation on an isolated QDH, it can be applied on the elementary cell of the QDH array. It means that method performances are not affected, as long as the invertibility condition is well satisfied.

In this section, we study the influence of geometrical parameters of the QDH array on its band structure. The analysis is based on the variation of the array period L, QDH width W and height H. In this study, the wetting layer thickness is set to $t_W = 0.5$ nm. However, the influence of the wetting layer thickness is also included in the discussion. In the analysis we vary one parameter at time, while other two are fixed and set to some average value. All calculations are performed for at least two different periods L, where one corresponds to large, while the others are for small W/L ratio. First, we study InAs/InAlGaAs QDH array, latticed matched to InP, and then QDH array based on InAs/GaAs which provides much deeper well.

Fig. 3 shows the miniband profile versus the array period L for two fitting functions, given by Eq. (7) [Figs. 3(a), 3(c), 3(f)] and Eq. (6) [Figs. 3(b), 3(d), 3(e), 3(g), 3(h)] for InAs/InAlGaAs QDH array. The QDH width is set to $W = 7$ nm, therefore for the range of period L from 8 to 20 nm it is more suitable to use Atanh-mapping since the ratio W/L is relatively large. For larger L, W/L ratio is smaller and much better fitting can be achieved by using Gauss-mapping. It can be seen that for densely packed QDHs there is a single and wide miniband [Fig. 3(a), $L < 12$ nm], which becomes narrower for increased period of the array and converges to the ground discrete state for $L > 25$ nm [Fig. 3(b)]. The coupling of QDHs also leads to formation of higher minibands, which become bound minibands for sufficiently large L ($L > 12$ nm). In other words, the excited minibands are part of the continuum for positive energies, i.e., small array periods. However, for large L, due to decreased quantum-mechanical coupling, these excited minibands become bound and narrower with respect to energy and tend to converge to the discrete excited states as the period increases. Finally, in the case of weak coupling between QDHs, i.e. for large L corresponding to almost isolated dashes, the band structure of the QDH array comprises one discrete state and wide band, consisting on a few almost joined minibands, close to the top of the well.

The variation of the QDH height H shows that for densely packed array, for which the ratio W/L is relatively large [Fig. 3(c)], height variation slightly affects the ground miniband width, especially for larger H-values. This result is not surprising, since the QDH coupling and consequently the miniband width depends on horizontal distance between the adjacent dashes (i.e., L or W) rather than on their vertical size. On the other hand, the variation of the QDH height H,

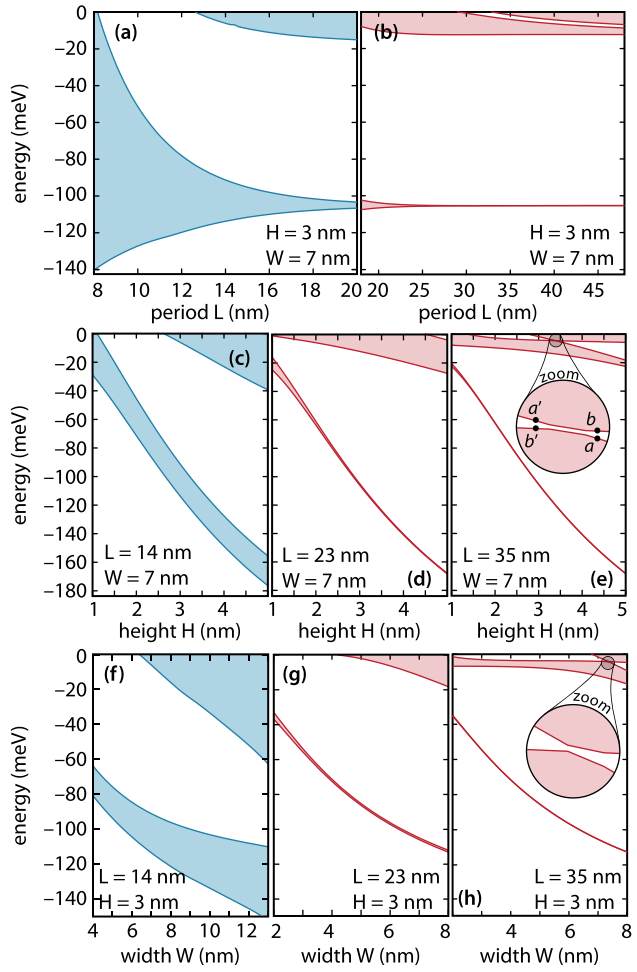

FIG. 3. The miniband structure for the periodic InAs/InGaAlAs QDH array with $t_W = 0.5$ nm with respect to (a)-(b) period L, (c)–(e) QDH height H, and (f)–(h) QDH width W. The miniband structure in (a), (c), and (f) correspond to QDH arrays obtained by fitting with Atanh-mapping, while those in (b), (d), (e), (g), and (h) correspond to the QDH arrays obtained by fitting with Gauss-mapping. Insets show zero-band-gap region between 2nd and 3rd miniband.

representing the QDH dimension in the direction of stronger confinement, leads to pronounced variation of the miniband energy. Similarly as for an electron in the infinitely deep quantum well, energy of which is inversely proportional to the square of the well width, the QDH miniband energy varies more rapidly with thickness variation for thinner than for thicker wells. Thus variation of the QDH height causes sudden change of the miniband energy. The dependence of the ground miniband width on H is, to some extent, different for relatively large L-values [Figs. 3(d) and 3(e)], since the miniband is already very narrow and its width slightly decreases with increase of H only for small H (1–2 nm). The reason is that increased H provides more space for the wavefunctions, which expand in the y- rather than in the x-direction, and in such way effectively reduces coupling among the dashes.

The increase of the dash width W, similarly as the increase of H, leads to the decrease of miniband energy. However, the width increase, for large W/L ratio, leads to the increase of the ground miniband width [Fig. 3(f)]. As a matter of fact, the width increase effectively decreases the period L, since the lateral sides of dashes come closer to each other [c.f. Fig. 2(a)]. As a result, the ground miniband becomes wider with increase of the QDH width. For smaller W/L ratio or large L, the QDH width weakly affects width of the minibands [Figs. 3(g) and 3(h)], although they decrease with W.

For sufficiently large L, the miniband dependence on width and height exhibits zero miniband gap effect (ZMBG), which can be observed for excited minibands, close to the top of the well [insets in Figs. 3(e) and 3(h)]. This effect is followed by miniband anticrossing. In other words, for the critical dimensions of QDH, the character of the top of the lower miniband is exchanged with the bottom of the higher miniband. The effect can be seen only for larger L, since the excited minibands, which are close to the well top, split due to the decrease of coupling, providing more minibands with smaller width. The effect can be also found in the case of variation of L, although it is not shown in figures.

The effect of zero miniband gap had been previously found in one-dimensional effective-mass superlattices.[16] It was shown that the effect can be noticed only for the minibands in the barrier (above the top of the well), in the case of variation of transversal, i.e., in-plane wave-vector k_t. The analytical treatment, which can be applied for the one-dimensional superlattices case, shows that the effect occurs for a certain conditions satisfied by the well and barrier width, and their corresponding effective masses. However, in the case of QDH array, the problem seems to be too complicated for analytical treatment. As it is shown in Fig. 3, the occurrence of the ZMBG effect depends on all three parameters (L, W, H). By using our numerical technique, we find that plots similar to Fig. 3 corresponding to $k_z > 0$ exhibit the shift of the ZMBG toward larger dimensions, i.e., larger L, W and H. The reason for this is the difference between the effective masses in the barrier and the well. Since the effective mass in the barrier is larger than the mass in the well, the increase of k_z effectively decreases the well depth, leading to weaker variation of subbands energy with dash dimension, than for $k_z = 0$. As a result, for $k_z > 0$, the ZMBG occurs for larger QDH dimensions, than for $k_z = 0$.

The presence of the wetting layer allows the barrier minibands to sink into the well and to exhibit the effect of zero miniband gap for energies for which the effect is not usually expected. Our calculation shows that the increase of the WL thickness increases the dash coupling and leads to the increase of the minibands width, their number and depth in the well. On the other hand, the decrease of the wetting layer to zero shows that the miniband structure almost completely disappears for large L, leaving only discrete energies. Consequently, the ZMBG effect is also vanishing in this case.

The ZMBG effect is followed by the anticrossing phenomenon, which is closely investigated in the case of height variation [zoom in Fig. 3(e)]. Fig. 4 shows the wavefunctions at the bottom of the 3rd and at the top of the 2nd miniband, for two height values, $H = 3.2$ nm and $H = 3.6$ nm, close to the critical height $H = 3.4$ nm, for which the zero miniband gap occurs. The boundary conditions at the extremes of the particular miniband (at its top and the bottom) have different sign of the phase shift factor $\exp(\imath KL)$, which can be $+1$ or

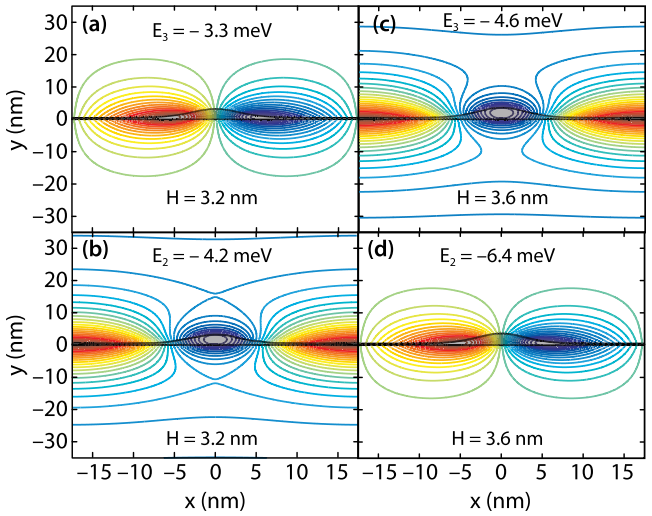

FIG. 4. Profile of the wavefunctions for QDH with $L = 35$ nm, $W = 7$ nm and $H = 3.2$ nm (a) at the bottom of the 3rd and (b) at the top of the 2nd miniband. (c) and (d): Same for $H = 3.6$ nm, respectively.

-1, depending on the miniband order. In addition, the sign of the phase factor, for the particular miniband extreme, according to the one-dimensional Kronig-Penney model, should alternate for adjacent minibands. According to this, the top of the 2nd and the bottom of the 3rd miniband should both correspond to the same, in this case, positive phase factor ($+1$). In principle, the wavefunction of the higher miniband should have different parity or more precisely, larger number of nodes in one or the other confinement direction, than the lower miniband. Figs. 4(a) and 4(b) representing the wavefunctions of the states denoted by a' and b' in the inset of Fig. 3(e), show that the wavefunctions corresponding to height smaller than the critical ($H = 3.2$ nm) do not follow this rule. However, for heights larger than the critical [$H = 3.6$ nm, points b and a in the inset of Fig. 3(e)] the rule applies again [Figs. 4(c) and 4(d)]. This means that for the states at the top and the bottom of the adjacent minibands, for which the ZMBG occurs, swap the character, i.e., wavefunctions parity, while keeping the same phase factor.

In order to further investigate minibands in the QDH array, we calculate the band structure for deeper wells, which occur in InAs/GaAs QDH array. Fig. 5 shows the miniband profile versus dash period L, for larger W/L ratio [Fig. 5(a)] with fitting function given by Eq. (7), and for smaller W/L, corresponding to the fitting function (6) [Fig. 5(b)]. It can be seen that the number of minibands is increased, as one may expect, compared to the previous material system. In addition, the minibands more rapidly converge to discrete states with the increase in L. Similar results are obtained for variation of H [Fig. 5(c)–5(e)] and W [Fig. 5(f)–5(h)]. It should be noted that the effect of zero miniband gap is quite common in deeper wells. As shown in Figs. 5(e) and 5(h), it can occur more than once for particular miniband and cause alternation of the wavefunction parity for the considered range of geometrical parameters.

The material system of InAs/GaAs represents better environment for explanation of the ZMBG effect, than the previous one. In order to qualitatively explain the effect we closely inspect Fig. 5(h) and the anticrossing of the 2nd and

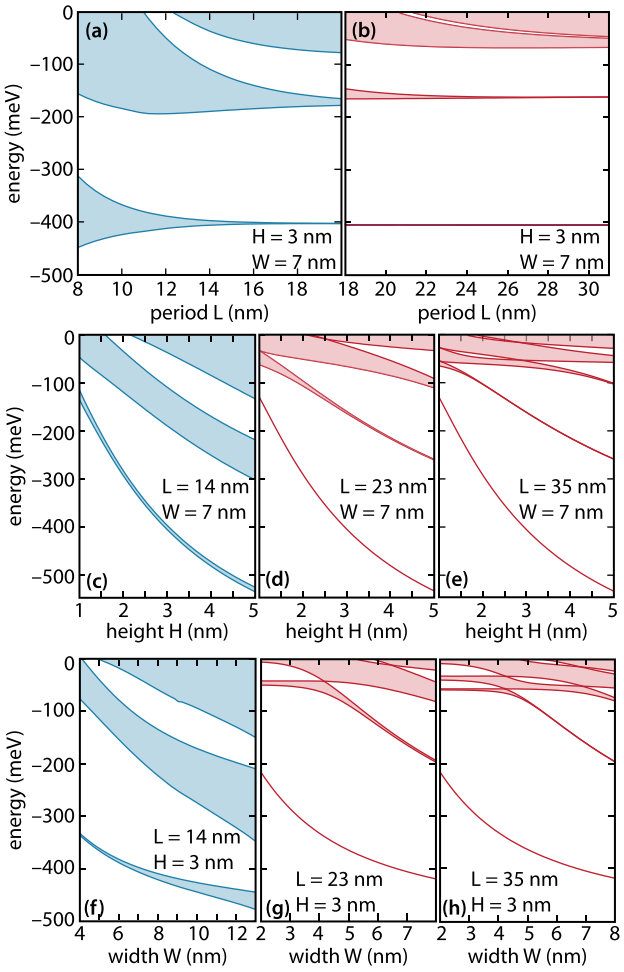

FIG. 5. The miniband structure for the periodic InAs/GaAs QDH array with $t_W = 0.5$ nm with respect to (a)–(b) period L, (c)–(e) QDH height H, and (f)–(h) QDH width W. The miniband structure in (a), (c), and (f) correspond to the QDH arrays obtained by fitting with Atanh-mapping, while those in (b), (d), (e), (g), and (h) correspond to the QDH arrays obtained by fitting with Gauss-mapping.

3rd miniband shown as schematics in Fig. 6. We start with small QDH widths ($W < 3$ nm), for which the wavefunctions of the 2nd and 3rd miniband are mainly situated in the wetting layer. This can be seen in the left column of Fig. 6 showing profiles of the wavefunctions for $W = 2.5$ nm. The widths of the minibands are very narrow. This is due to the fact that array period L is large enough that modulo of the wavefunctions corresponding to the extremes of the miniband are very similar, although the wavefunctions themselves have different parity due to the opposite phase factors. The increase of the QDH width provides more space for the wavefunction to accommodate into the QDH region. As long as the wavefunction is mainly situated into the wetting layer, the increase of the QDH width does not affect the miniband energy. Once the QDH width is large enough to accommodate a considerable part of the wavefunction, the increase of the QDH width will decrease the energy of the miniband or its extreme. However, due to different parity, the extremes of a miniband or the closest extremes of two adjacent minibands, have different critical widths for which their energy begins to decrease. For example, the top of the 2nd miniband has the same phase factor as the bottom of the 3rd miniband.

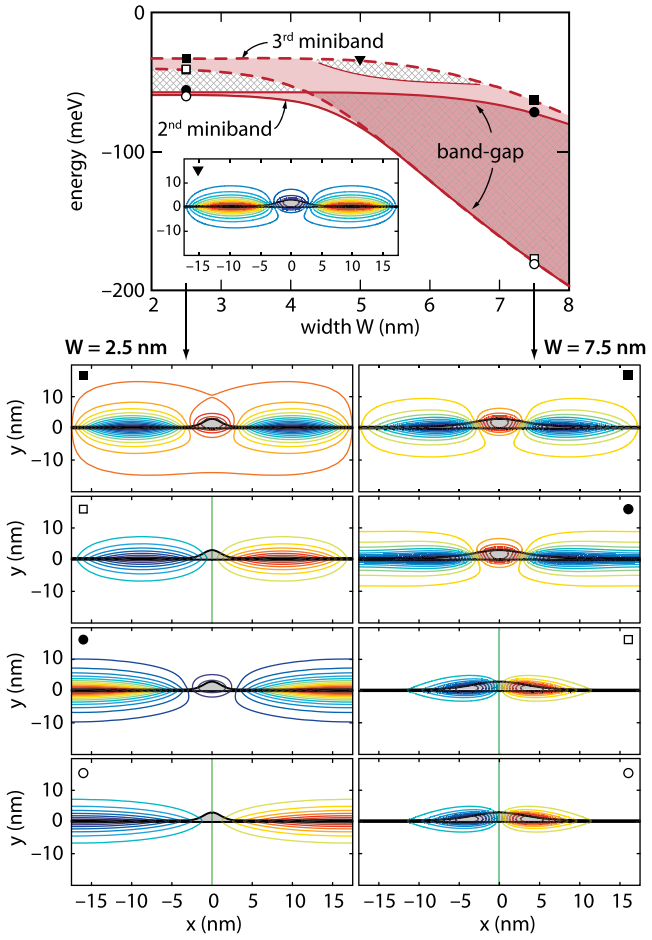

FIG. 6. Schematics of the ZMBG and anti-crossing effect between the 2nd and 3rd miniband for InAs/GaAs QDH array with $L = 35$ nm and $H = 3$ nm with respect to variation of QDH width W. Wavefunction profiles corresponding to $W = 2.5$, 5 and 7.5 nm are denoted with open and solid square, triangle, and dot markers.

In spite of that, the parity of these two wavefunctions is different, similarly as the parity of the top and the bottom of any of these two minibands. Due to larger number of nodes in the wavefunction (solid dot marker and corresponding wavefunction for $W = 2.5$ nm) the top of the 2nd miniband begins to decrease for larger widths than the bottom of the 3rd miniband, which wavefunction has smaller number of nodes (open square marker and corresponding wavefunction for $W = 2.5$ nm). Thus, for widths for which the bottom of the 3rd miniband decreases, the top of the 2nd miniband is almost constant. As a result, these two extremes approach each other, leading to the anticrossing of the minibands and the swap of the wavefunctions parity (solid dot and open square markers and corresponding wavefunctions profiles for $W = 7.5$ nm).

In general, the band structure at the top of the well consists of densely packed minibands, which represent a kind of so-called bound continuum. It can be expected that careful design of such complex continuum may provide efficient capture and relaxation of carriers into the QDH well, which might be essential for applications comprising optical transitions.

IV. CONCLUSIONS

The paper presents an efficient method for the calculation of the miniband structure of one-dimensional periodic QDH array, and based on the method, provides an analysis of its miniband character versus geometrical parameters. The method is a combination of the coordinate transformation of the QDH array and its vicinity into rectangular computational domain and the single-band Schrödinger equation solving in this domain by the finite differences method. The efficiency of the method is the result of array periodicity and carefully designed periodic fitting functions used for the coordinate transformation. The study of the minibands of the QDH array shows that miniband width is strongly related to the array period L and the wetting layer thickness t_W, although the width of QDHs may have significant impact for large ratio of the QDH width and array period. The miniband energy, on the other hand, considerably depends on the width W and the height H of QDHs in the array. For large periods L and some critical dimensions L, H or W, adjacent minibands in QDH array may exhibit the phenomenon of zero miniband gap, which is followed by the swap of the miniband character in its vicinity. Due to the wetting layer, higher minibands are clustered in the vicinity of the well top, providing a kind of the "bound continuum," which might be relevant for control of capture and relaxation of excited carriers.

ACKNOWLEDGMENTS

This work is supported by the Serbian Ministry of Science under project Photonics Components and Systems, No. 171011.

[1]E. A. Zibik, T. Grange, B. A. Carpenter, N. E. Porter, R. Ferreira, G. Bastard, D. Stehr, S. Winnerl, M. Helm, H. Y. Liu, M. S. Skolnick, and L. R. Wilson, Nature Mater. **8**, 803 (2009).
[2]V. Liverini, A. Bismuto, L. Nevou, M. Beck, and J. Faist, Appl. Phys. Lett. **97**, 221109 (2010).
[3]J. H. Wei and K. S. Chan, J. Appl. Phys. **97**, 123524 (2005).
[4]H. Dery, E. Benisty, A. Epstein, R. Alizon, V. Mikhelashvili, G. Eisenstein, R. Schwertberger, D. Gold, J. P. Reithmaier, and A. Forchel, J. Appl. Phys. **95**, 6103 (2004).
[5]M. Gioannini, IEEE J. Quantum Electron. **40**, 364 (2004).
[6]J. V. Crnjanski and D. M. Gvozdić, Acta Phys. Pol. A **116**, 668 (2009).
[7]J. V. Crnjanski and D. M. Gvozdić, Appl. Phys. Lett. **97**, 091906 (2010).
[8]J. V. Crnjanski, Phys. Scr. **T149**, 014034 (2012).
[9]M. Gioannini, IEEE J. Quantum Electron. **42**, 331 (2006).
[10]P. Miska, J. Even, C. Platz, B. Salem, T. Benyattou, C. Bru-Chevalier, G. Guillot, G. Bremond, Kh. Moumanis, F. H. Julien, O. Marty, C. Monat, and M. Gendry, J. Appl. Phys. **95**, 1074 (2004).
[11]A. Sauerwald, T. Kummell, G. Bacher, A. Somers, R. Schwertberger, J. P. Reithmaier, and A. Forchel, Appl. Phys. Lett. **86**, 253112 (2005).
[12]B. M. Stupovski, J. V. Crnjanski, and D. M. Gvozdić, Comput. Phys. Commun. **182**, 289 (2011).
[13]I. Vurgaftman, J. R. Meyer, and L. R. Ram-Mohan, J. Appl. Phys. **89**, 5815 (2001).
[14]T.-M. Hwang, W.-W. Lin, W.-C. Wang, and W. Wang, J. Comput. Phys. **196**, 208 (2004).
[15]T.-M. Hwang, W.-C. Wang, and W. Wang, J. Comput. Phys. **226**, 754 (2007).
[16]V. Milanović and Z. Ikonić, Phys. Rev. B **37**, 7125 (1988).

Arch. Math.

https://doi.org/10.1007/s00013-020-01511-x

Archiv der Mathematik

Existence of Riemannian metrics with positive biorthogonal curvature on simply connected 5-manifolds

Boris Stupovski and Rafael Torres

Abstract. Using the recent work of Bettiol, we show that a first-order conformal deformation of Wilking's metric of almost-positive sectional curvature on $S^2 \times S^3$ yields a family of metrics with strictly positive average of sectional curvatures of any pair of 2-planes that are separated by a minimal distance in the 2-Grassmanian. A result of Smale allows us to conclude that every closed simply connected 5-manifold with torsion-free homology and trivial second Stiefel–Whitney class admits a Riemannian metric with a strictly positive average of sectional curvatures of any pair of orthogonal 2-planes.

Mathematics Subject Classification. Primary 53C20, 53C21, Secondary 53B21.

Keywords. Positive biorthogonal curvature, Biorthogonal curvature, 5-manifolds.

1. Introduction and main results. Let (M, g) be a compact Riemannian n-manifold and let $\sec_g$ be the sectional curvature of the metric. We often abuse notation and denote the Riemannian metric by (M, g) as well. For each 2-plane

$$\sigma \in \mathrm{Gr}_2(T_pM) = \{X \wedge Y \in \Lambda^2 T_pM : ||X \wedge Y||^2 = 1\}, \tag{1.1}$$

let $\sigma^\perp \subset T_pM$ be its orthogonal complement. That is, there is a g-orthogonal direct sum decomposition $\sigma \oplus \sigma^\perp = T_pM$ at a point $p \in M$.

Definition 1. The biorthogonal curvature of a 2-plane $\sigma \in \mathrm{Gr}_2(T_pM)$ is

$$\sec_g^\perp(\sigma) := \min_{\substack{\sigma' \in \mathrm{Gr}_2(T_pM) \\ \sigma' \subset \sigma^\perp}} \frac{1}{2}(\sec_g(\sigma) + \sec_g(\sigma')) \tag{1.2}$$

(cf. [3, Section 5.4]). We say that (M, g) has positive biorthogonal curvature $\sec_g^\perp > 0$ if (1.2) is positive for every $\sigma \in \mathrm{Gr}_2(T_pM)$ at every point $p \in M$.

Published online: 11 August 2020

A stronger curvature condition is the following. Choose a distance on the Grassmanian bundle $\mathrm{Gr}_2(TM)$ that induces the standard topology.

Definition 2. The distance curvature of a 2-plane $\sigma \subset T_pM$ is

$$\sec_g^\theta(\sigma) := \min_{\substack{\sigma' \in \mathrm{Gr}_2(T_pM) \\ \mathrm{dis}(\sigma,\sigma') \geq \theta}} \frac{1}{2}(\sec_g(\sigma) + \sec_g(\sigma')) \tag{1.3}$$

for each $\theta > 0$ (cf. [3, Section 5.2]). We say that (M, g^θ) has positive distance curvature $\sec_{g^\theta} > 0$ if for every $\theta > 0$, there is a Riemannian metric (M, g^θ) for which (1.3) is positive for every $\sigma \in \mathrm{Gr}_2(T_pM)$ at every point $p \in M$.

Bettiol [4] classified up to homeomorphism closed simply connected 4-manifolds that admit a Riemannian metric of positive biorthogonal curvature by constructing metrics of positive distance curvature on $S^2 \times S^2$ [2, Theorem, Proposition 5.1], [3, Theorem 6.1], and showing that positive biorthogonal curvature is a property that is closed under connected sums [3, Proposition 7.11], [4, Proposition 3.1].

In this paper, we extend Bettiol's results to dimension five. More precisely, we build upon Bettiol's work and show that an application of a first-order conformal deformation to Wilking's metric $(S^2 \times S^3, g_W)$ of almost-positive sectional curvature [11] yields the main result of this note.

Theorem A. *For every $\theta > 0$, there is a Riemannian metric $(S^2 \times S^3, g^\theta)$ such that*

(a) $\sec^\theta_{g^\theta} > 0$;
(b) there is a limit metric g^0 such that $g^\theta \to g^0$ in the C^k-topology as $\theta \to 0$ for $k \geq 0$;
(c) g^θ is arbitrarily close to Wilking's metric g_W of almost-positive curvature in the C^k-topology for $k \geq 0$;
(d) $\mathrm{Ric}_{g^\theta} > 0$;
(e) there is a 2-plane $\sigma \in \mathrm{Gr}_2(T_pS^2 \times S^3)$ with $\sec_{g^\theta}(\sigma) < 0$;

In particular, there is a Riemannian metric of positive biorthogonal curvature on $S^2 \times S^3$.

The next corollary is a consequence of coupling Theorem A with a classification result of Smale [8].

Corollary B. *Every closed simply connected 5-manifold with torsion-free homology and zero second Stiefel–Whitney class admits a Riemannian metric of positive biorthogonal curvature.*

The hypothesis imposed on the homology and the second Stiefel–Whitney class of the manifolds of Corollary B are technical in nature; cf. Remark 2. Indeed, an examination of the canonical metric on the Wu manifold yields the following proposition.

Proposition C. *The symmetric space metric $(\mathrm{SU}(3)/\mathrm{SO}(3), g)$ has positive biorthogonal curvature.*

The Wu manifold has second homology group of order two and nontrivial second Stiefel–Whitney class.

2. Constructions of Riemannian metrics of positive biorthogonal curvature.

2.1. Wilking's metric of almost-positive curvature on $S^2 \times S^3$. We follow the exposition in [11, Section 5] to describe Wilking's construction of a metric of almost-positive curvature on the product of projective spaces $\mathbb{R}P^2 \times \mathbb{R}P^3$ and its pullback to $S^2 \times S^3$ under the covering map; see [12, Section 5] for a discussion relating these two constructions.

The unit tangent sphere bundle of the 3-sphere

$$T_1(S^3) = S^2 \times S^3, \tag{2.1}$$

embeds into $\mathbb{R}^4 \times \mathbb{R}^4 = \mathbb{H} \times \mathbb{H}$ as a pair of orthogonal unit quaternions

$$S^3 \times S^2 = \{(p, v) \in \mathbb{H} \times \mathbb{H} : |p| = |v| = 1, \langle p, v\rangle = 0\} \subset \mathbb{H} \times \mathbb{H}, \tag{2.2}$$

where $\langle x, y\rangle = \mathrm{Re}(\bar{x}y)$, $|x|^2 = \langle x, x\rangle$, and $\bar{x}$ denotes the quaternion conjugation of x. The group $G = \mathrm{Sp}(1) \times \mathrm{Sp}(1) \simeq S^3 \times S^3$ acts on $S^2 \times S^3$ by

$$(q_1, q_2) \star (p, v) = (q_1 p \bar{q}_2, q_1 v \bar{q}_2) \tag{2.3}$$

for $q_1, q_2 \in \mathrm{Sp}(1)$ and $(p, v) \in S^2 \times S^3$. This action is effectively free and transitive. The isotropy group of the point $(1, i) \in S^2 \times S^3$ is

$$H = \{(e^{i\phi}, e^{i\phi}) \in \mathrm{Sp}(1) \times \mathrm{Sp}(1)\} \subset G. \tag{2.4}$$

Thus, $S^2 \times S^3 \simeq G/H$ is a homogeneous space.

In order to put a metric on $S^2 \times S^3$, Wilking first defines a left invariant metric g on $G = \mathrm{Sp}(1) \times \mathrm{Sp}(1)$ as follows. Let

$$g_0((X, Y), (X', Y')) = \langle X, Y\rangle + \langle X', Y'\rangle, \tag{2.5}$$

for $(X, Y), (X', Y') \in \mathfrak{sp}(1) \oplus \mathfrak{sp}(1) = \mathrm{Im}(\mathbb{H}) \oplus \mathrm{Im}(\mathbb{H})$, denote a bi-invariant metric. In terms of g_0, the metric g is

$$g((X, Y), (X', Y')) = g_0(\Phi(X, Y), (X', Y')), \tag{2.6}$$

where Φ is a g_0-symmetric, positive definite endomorphism of $\mathfrak{sp}(1) \oplus \mathfrak{sp}(1)$ given by

$$\Phi = \mathrm{Id} - \frac{1}{2}P, \tag{2.7}$$

and P is the g_0-orthogonal projection onto the diagonal subalgebra

$$\Delta\mathfrak{sp}(1) \subset \mathfrak{sp}(1) \oplus \mathfrak{sp}(1); \tag{2.8}$$

see [11, p. 125].

Wilking's doubling trick guarantees the existence of a diffeomorphism

$$G/H \simeq \Delta G \backslash G \times G / \{1_G\} \times H, \tag{2.9}$$

where $\Delta G\backslash$ denotes the quotient by the left diagonal action of G on $G \times G$ and H acts on the second factor from the right. Consider the product $(G \times G, g + g)$ (cf. (2.6)) and the induced metric on $S^2 \times S^3 \simeq \Delta G \backslash G \times G / \{1_G\} \times H$ that we denote by g_W. That is, Wilking's metric $(S^2 \times S^3, g_W)$ is the metric that makes the quotient submersion

$$(G \times G, g \oplus g) \to (\Delta G \backslash G \times G / \{1_G\} \times H, g_W) \tag{2.10}$$

into a Riemannian submersion. Wilking has shown that $(S^2 \times S^3, g_W)$ has almost-positive curvature, with flat 2-planes located on two hypersurfaces. These hypersurfaces are both diffeomorphic to $S^2 \times S^2$, and they intersect along an $\mathbb{R}P^3$ [11, Corollary 3, Proposition 6]. However, except for points that lie on four disjoint copies of S^2 inside these two hypersurfaces, there is a unique flat 2-plane. At each point in these four 2-spheres, there is a one parameter family of flat 2-planes and neither the distance curvature nor the biorthogonal curvature of the metric g_W are strictly positive at any of these points.

3. Proofs.

3.1. Proof of Theorem A. We follow Bettiol's construction of metrics of positive distance curvature on $S^2 \times S^2$ [2, Theorem], [3, Theorem 6.1], and apply a first-order conformal deformation to Wilking's metric $(S^2 \times S^3, g_W)$ that was described in Section 2.1. This yields metrics of positive distance curvature as in Definition 2, which converge to a metric g^0 as θ tends to zero in the C^k-topology.

Definition 3. Let (M, g) be a compact Riemannian manifold, then, for any function $\phi : M \to \mathbb{R}$, and for any small enough $s > 0$, the following is also a Riemannian metric on M

$$g_s = (1 + s\phi)g, \tag{3.1}$$

called the first-order conformal deformation of g.

The variation of sectional curvature of a metric under the first order conformal deformation is given by the following lemma [9]; cf. [3, Chapter 3, Corollary 3.4].

Lemma 1. *Let (M, g) be a Riemannian manifold with sectional curvature $\sec_g \geq 0$, and let $X, Y \in T_pM$ be g-orthonormal vectors such that $\sec_g(X \wedge Y) = 0$. Consider a first-order conformal deformation $g_s = (1+s\phi)g$ of g. The first variation of $\sec_{g_s}(X \wedge Y)$ is*

$$\frac{\mathrm{d}}{\mathrm{d}s}\sec_{g_s}(X \wedge Y)|_{s=0} = -\frac{1}{2}\mathrm{Hess}\,\phi(X, X) - \frac{1}{2}\,\mathrm{Hess}\,\phi(Y, Y). \tag{3.2}$$

We will also need the following elementary fact [3, Chapter 3, Lemma 3.5].

Lemma 2. *Let $f : [0, S] \times K \to \mathbb{R}$ be a smooth function, where $S > 0$ and K is a compact subset of a manifold. Assume that $f(0, x) \geq 0$ for all $x \in K$, and $\frac{\partial f}{\partial s} > 0$ if $f(0, x) = 0$. Then there exists $s_* > 0$ such that $f(s, x) > 0$ for all $x \in K$ and $0 < s < s_*$.*

Wilking's metric $(S^2 \times S^3, g_W)$ has positive sectional curvature away from a hypersurface Z; see the discussion at the end of Section 2.1. The biorthogonal and distance curvatures are positive inside Z except for points that lie in four disjoint copies of S^2. Every point in these four 2-spheres carries an S^1 worth of flat 2-planes. Denote these four 2-spheres by

$$\{S_i^2 : i = 1, 2, 3, 4\}. \tag{3.3}$$

We only deform Wilking's metric near these four submanifolds. Let

$$\chi_i : S^2 \times S^3 \to \mathbb{R} \tag{3.4}$$

denote a bump function of S_i^2, i.e., a nonnegative function that is identically zero outside a tubular neighborhood of S_i^2, and identically one in a smaller tubular neighborhood of S_i^2. Finally, we define four functions

$$\{\psi_i : S^2 \times S^3 \to \mathbb{R} : i = 1, 2, 3, 4\} \tag{3.5}$$

as

$$\psi_i(p) = \mathrm{dist}_{g_W}(p, S_i^2)^2 \tag{3.6}$$

for $p \in S^2 \times S^3$, where dist_{g_W} is the metric distance function on $(S^2 \times S^3, g_W)$. Let $\phi : S^2 \times S^3 \to \mathbb{R}$ be a function defined as

$$\phi = -\chi_1\psi_1 - \chi_2\psi_2 - \chi_3\psi_3 - \chi_4\psi_4, \tag{3.7}$$

and consider the first-order conformal deformation of g_W given by

$$g_s = (1 + s\phi)g_W. \tag{3.8}$$

Note that at a point $p \in S_i^2$, we have

$$\mathrm{Hess}\,\phi(X, X) = -\mathrm{Hess}\,\psi_i(X, X) = -2g_W(X_\perp, X_\perp)^2 = -2\|X_\perp\|_{g_W}^2, \tag{3.9}$$

where $X_\perp$ denotes the component of X perpendicular to S_i^2. For each $\theta > 0$, consider the compact subset of $(S^2 \times S^3) \times \mathrm{Gr}_2(T(S^2 \times S^3)) \times \mathrm{Gr}_2(T(S^2 \times S^3))$ given by

$$K_\theta := \{(p, \sigma, \sigma') : \sigma, \sigma' \in \mathrm{Gr}_2(T_p(S^2 \times S^3)), \mathrm{dist}(\sigma, \sigma') \geq \theta\}, \tag{3.10}$$

and define

$$\begin{gathered} f : [0, S] \times K_\theta \to \mathbb{R}, \\ f(s, (p, \sigma, \sigma')) := \frac{1}{2}(\sec_{g_s}(\sigma) + \sec_{g_s}(\sigma')). \end{gathered} \tag{3.11}$$

Notice that $f(0, (p, \sigma, \sigma')) \geq 0$ since $\sec_{g_s} \geq 0$. Furthermore, $f(0, (p, \sigma, \sigma')) = 0$ only for

$$p \in S_1^2 \cup S_2^2 \cup S_3^2 \cup S_4^2 \tag{3.12}$$

since these are the only points of $S^2 \times S^3$ that have vanishing biorthogonal and distance curvatures. Let (p, σ, σ') be such that $f(0, (p, \sigma, \sigma')) = 0$ and let $\sigma = X \wedge Y$ and $\sigma' = Z \wedge W$, where X, Y are g_W-orthonormal, and Z, W are g_W-orthonormal. Then, by Lemma 1 and equation (3.9), at these points of K_θ, we have

$$\begin{aligned} \frac{\partial f}{\partial s}|_{s=0} &= \frac{\mathrm{d}}{\mathrm{d}s}(\sec_{g_s}(X \wedge Y) + \sec_{g_s}(Z \wedge W))|_{s=0} \\ &= -\frac{1}{2}\mathrm{Hess}\,\phi(X, X) - \frac{1}{2}\mathrm{Hess}\,\phi(Y, Y) - \frac{1}{2}\mathrm{Hess}\,\phi(Z, Z) - \frac{1}{2}\mathrm{Hess}\,\phi(W, W) \\ &= \|X_\perp\|_{g_W}^2 + \|Y_\perp\|_{g_W}^2 + \|Z_\perp\|_{g_W}^2 + \|W_\perp\|_{g_W}^2 > 0. \end{aligned} \tag{3.13}$$

The previous expression is strictly greater than zero. Indeed, since $X \wedge Y$ and $Z \wedge W$ are different 2-planes, $\mathrm{span}\{X, Y, Z, W\}$ is at least three-dimensional while the submanifolds (3.3) are two-dimensional. Hence, at least one of the perpendicular components $X_\perp, Y_\perp, Z_\perp, W_\perp$ is nonzero and (3.13) is greater

than zero. Since the assumptions of Lemma 2 for the function (3.11) are satisfied, we conclude that there is an s_* such that $f(s,(p,\sigma,\sigma')) > 0$ for all $(p,\sigma,\sigma') \in K_\theta$ and $0 < s < s_*$. This is precisely the condition $\sec^\theta_{g_s} > 0$ of item (a) of Theorem A. The claims of item (b) and item (c) follow from our construction; cf. [2]. The claim of item (d) follows from [2, Proposition 4.1]. As Bettiol observed in his construction of metrics of positive distance curvature on $S^2 \times S^2$ [2, Section 4.4], for every $\theta > 0$, there are 2-planes in $(S^2 \times S^3, g^\theta)$ with negative sectional curvature. This completes the proof of Theorem A. □

Remark 1. The metrics $(S^2 \times S^3, g^\theta)$ of positive distance curvature can be made invariant under the action of certain Deck transformations including the product $\mathbb{Z}/2 \oplus \mathbb{Z}/2$-action. Indeed, it is possible to perform a local conformal deformation on the orbit space $(\mathbb{R}P^2 \times \mathbb{R}P^3, g_W)$ equipped with Wilking's metric of almost positive curvature, and a similar statement to Theorem A holds for $(\mathbb{R}P^2 \times \mathbb{R}P^3, g^\theta)$; cf. [2, Section 4.6].

3.2. Proof of Corollary B. We will use a case of the classification up to diffeomorphism of simply connected 5-manifolds with vanishing second Stiefel–Whitney class due to Smale [8, Theorem A].

Theorem 1. *A closed simply connected 5-manifold M with torsion-free homology $H_2(M;\mathbb{Z}) = \mathbb{Z}^k$ and zero second Stiefel–Whitney class $w_2(M) = 0$ is determined up to diffeomorphism by its second Betti number $b_2(M)$. In particular, M is diffeomorphic to a connected sum*

$$\{S^5 \# k(S^2 \times S^3) : k = b_2(M)\}. \tag{3.14}$$

Theorem A and Bettiol's result regarding the positivity of biorthogonal curvature under connected sums [3, Proposition 7.11] imply that every 5-manifold in the set (3.14) admits a Riemannian metric of positive biorthogonal curvature. □

Remark 2. It is natural to ask if the hypothesis $w_2(M) = 0$ of Corollary B can be removed. Barden has shown that a closed simply connected 5-manifold with torsion-free second homology group is diffeomorphic to a connected sum of copies of $S^2 \times S^3$ and the total space $S^3 \widetilde{\times} S^2$ of the nontrivial 3-sphere bundle over the 2-sphere [1]. It is currently unknown if there is a metric of almost-positive sectional curvature on $S^3 \widetilde{\times} S^2$. Unlike $S^2 \times S^3$, the nontrivial bundle does not arise as a biquotient that satisfies the symmetry hypothesis needed to apply Wilking's doubling trick; see DeVito's classification of free circle actions on $S^3 \times S^3$ in [5].

3.3. Proof of Proposition C. The symmetric space metric on $\mathrm{SU}(3)/\mathrm{SO}(3)$ is the metric that makes the canonical surjection

$$\begin{aligned} \pi : \mathrm{SU}(3) &\to \mathrm{SU}(3)/\mathrm{SO}(3), \\ u &\mapsto u\mathrm{SO}(3), \end{aligned} \tag{3.15}$$

into a Riemannian submersion, where $\mathrm{SU}(3)$ is equipped with a bi-invariant metric. The left action of $\mathrm{SU}(3)$ on $\mathrm{SU}(3)/\mathrm{SO}(3)$ induced from the left multiplication on $\mathrm{SU}(3)$ by (3.15) is transitive and isometric for the symmetric space

metric. This means that we can study curvature at one point of SU(3)/SO(3) and isometrically translate the results to any other point. The Cartan decomposition that corresponds to SU(3)/SO(3)

$$T_e\mathrm{SU}(3) \simeq \mathfrak{su}(3) = \mathfrak{so}(3) \oplus \mathfrak{so}(3)^{\perp} \tag{3.16}$$

is orthogonal with respect to the bi-invariant metric and it is precisely the decomposition of $T_e\mathrm{SU}(3)$ into vertical and horizontal subspaces of the Riemannian submersion (3.15). Hence, we have

$$T_{\mathrm{SO}(3)}(\mathrm{SU}(3)/\mathrm{SO}(3)) \simeq \mathfrak{so}(3)^{\perp}. \tag{3.17}$$

To conclude that SU(3)/SO(3) has positive biorthogonal curvature, we need to show that no two flat 2-planes are orthogonal to each other. A result of Tapp [10, Theorem 1.1] implies that a 2-plane on SU(3)/SO(3) is flat if and only if its horizontal lift is flat. Thus, it is enough to consider horizontal flat 2-planes at the identity of SU(3).

A horizontal 2-plane $X \wedge Y \subset \mathfrak{so}(3)^{\perp}$ at the identity of SU(3) is flat if and only if $[X, Y] = 0$. Since the maximal number of linearly independent commuting matrices in $\mathfrak{su}(3)$ is two, every horizontal flat 2-plane corresponds to a maximal abelian subalgebra of $\mathfrak{so}(3)^{\perp}$

$$\mathrm{span}_{\mathbb{R}}\{X, Y\} = \mathfrak{a}_0 \subset \mathfrak{so}(3)^{\perp}. \tag{3.18}$$

By a fundamental fact about the Cartan decomposition, see [7, Proposition 7.29] for the precise statement, any two maximal abelian subalgebras of $\mathfrak{so}(3)^{\perp}$ are conjugate by an element of SO(3). This means that by fixing one maximal abelian subalgebra, or one horizontal flat 2-plane, we can parametrize all horizontal flat 2-planes by SO(3). In what follows, we will obtain an explicit parametrization of horizontal flat 2-planes at the identity of SU(3), and so a parametrization of flat 2-planes at a point of SU(3)/SO(3) by choosing a basis for $\mathfrak{su}(3)$, fixing a horizontal flat 2-plane and parametrizing SO(3) by Euler angles. We use this explicit parametrization to show that no two flat 2-planes can be orthogonal. For the basis of $\mathfrak{su}(3)$, we choose $\{-i\lambda_i\}_{i=1,\ldots,8}$, where the λ_i's are traceless, self-adjoint 3 by 3 matrices known as the Gell-Mann matrices [6]. The scalar product on $\mathfrak{su}(3)$ that corresponds to the bi-invariant metric is

$$\langle X, Y\rangle = -\frac{1}{2}\mathrm{Tr}(XY) \tag{3.19}$$

for $X, Y \in \mathfrak{su}(3)$ and the basis $\{-i\lambda_i\}_{i=1,\ldots,8}$ is orthonormal with respect to (3.19). The Cartan decomposition (3.16) in this basis is

$$\mathfrak{so}(3) = \mathrm{span}_{\mathbb{R}}\{-i\lambda_2, -i\lambda_5, -i\lambda_7\} \tag{3.20}$$

and

$$\mathfrak{so}(3)^{\perp} = \mathrm{span}_{\mathbb{R}}\{-i\lambda_1, -i\lambda_3, -i\lambda_4, -i\lambda_6, -i\lambda_8\}. \tag{3.21}$$

Matrices λ_3 and λ_8 are diagonal, so we use $-\lambda_3 \wedge \lambda_8$ for the reference horizontal flat 2-plane. Every horizontal flat 2-plane, $X \wedge Y$, with $X, Y \in \mathfrak{so}(3)^{\perp}$ such that $[X, Y] = 0$, can now be written as

$$X \wedge Y = -\mathrm{Ad}_r(\lambda_3 \wedge \lambda_8) \tag{3.22}$$

for some $r \in \mathrm{SO}(3)$. Suppose that $X \wedge Y$ and $X' \wedge Y'$ are two such 2-planes with $X \wedge Y$ given by (3.22) and $X' \wedge Y'$ by

$$X' \wedge Y' = -\mathrm{Ad}_{r'}(\lambda_3 \wedge \lambda_8) \tag{3.23}$$

for some $r' \in \mathrm{SO}(3)$. For the 2-planes (3.22) and (3.23) to be orthogonal, it is necessary and sufficient that the equations

$$\langle \mathrm{Ad}_r \lambda_3, \mathrm{Ad}_{r'} \lambda_3 \rangle = 0, \tag{3.24}$$
$$\langle \mathrm{Ad}_r \lambda_3, \mathrm{Ad}_{r'} \lambda_8 \rangle = 0, \tag{3.25}$$
$$\langle \mathrm{Ad}_r \lambda_8, \mathrm{Ad}_{r'} \lambda_3 \rangle = 0, \tag{3.26}$$

and

$$\langle \mathrm{Ad}_r \lambda_8, \mathrm{Ad}_{r'} \lambda_8 \rangle = 0 \tag{3.27}$$

hold. Using the Ad-invariance of the bi-invariant metric, equations (3.24), (3.25), (3.26), and (3.27) can be rewritten as

$$\langle \lambda_3, \mathrm{Ad}_{r^{-1}r'} \lambda_3 \rangle = 0, \tag{3.28}$$
$$\langle \lambda_3, \mathrm{Ad}_{r^{-1}r'} \lambda_8 \rangle = 0, \tag{3.29}$$
$$\langle \lambda_8, \mathrm{Ad}_{r^{-1}r'} \lambda_3 \rangle = 0, \tag{3.30}$$

and

$$\langle \lambda_8, \mathrm{Ad}_{r^{-1}r'} \lambda_8 \rangle = 0. \tag{3.31}$$

We now use the Euler angle parametrization of $\mathrm{SO}(3)$ to write $r^{-1}r' \in \mathrm{SO}(3)$ as

$$r^{-1}r' = \exp(-i\lambda_2 x)\exp(-i\lambda_5 y)\exp(-i\lambda_2 z), \tag{3.32}$$

where $x, y, z \in \mathbb{R}$. Plugging (3.32) into equations (3.28), (3.29), (3.30), and (3.31) and calculating the traces explicitly, we find

$$\begin{aligned} 0 &= \langle \lambda_3, \mathrm{Ad}_{r^{-1}r'} \lambda_3 \rangle \\ &= \frac{1}{4}\cos(2x)\,(3 + \cos(2y))\cos(2z) - \sin(2x)\cos(y)\sin(2z), \end{aligned} \tag{3.33}$$

$$0 = \langle \lambda_3, \mathrm{Ad}_{r^{-1}r'} \lambda_8 \rangle = -\frac{\sqrt{3}}{2}\cos(2x)\sin^2(y), \tag{3.34}$$

$$0 = \langle \lambda_8, \mathrm{Ad}_{r^{-1}r'} \lambda_3 \rangle = -\frac{\sqrt{3}}{2}\cos(2z)\sin^2(y), \tag{3.35}$$

and

$$0 = \langle \lambda_8, \mathrm{Ad}_{r^{-1}r'} \lambda_8 \rangle = \frac{1}{4}(1 + 3\cos(2y))\,. \tag{3.36}$$

Equations (3.34), (3.35), and (3.36) imply $\cos^2(y) = 1/3$ and $\cos(2x) = \cos(2z) = 0$. Plugging this into equation (3.33), we obtain

$$\langle \lambda_3, \mathrm{Ad}_{r^{-1}r'} \lambda_3 \rangle \neq 0, \tag{3.37}$$

and conclude that there is no solution to the system given by equations (3.33), (3.34), (3.35), and (3.36). This shows that no two 2-flat planes are orthogonal. □

Acknowledgements. We thank the referee and Renato Bettiol for useful input that allowed us to significantly improve the paper. R.T. thanks Nicola Gigli for very helpful discussions during the production of the paper.

References

[1] Barden, D.: Simply connected five-manifolds. Ann. Math. **82**, 365–385 (1965)

[2] Bettiol, R.G.: Positive biorthogonal curvature on $S^2 \times S^2$. Proc. Amer. Math. Soc. **142**, 4341–4353 (2014)

[3] Bettiol, R.G.: On different notions of positivity of curvature, PhD thesis, University of Notre Dame (2015)

[4] Bettiol, R.G.: Four-dimensional manifolds with positive biorthogonal curvature. Asian J. Math. **21**, 391–396 (2017)

[5] DeVito, J.: The classification of simply connected biquotients of dimension at most 7 and 3 new examples of almost positively curved manifolds, PhD thesis, University of Pennsylvania (2011)

[6] Gell-Mann, M.: Symmetries of baryons and mesons. Phys. Rev. **125**, 1067–1084 (1962)

[7] Knapp, A.W.: Lie Groups: Beyond an Introduction, Progress in Mathematics, vol. 140, 2nd edn. Birkhäuser, Boston (2002)

[8] Smale, S.: On the structure of 5-manifolds. Ann. Math. **75**(2), 38–46 (1962)

[9] Strake, M.: Curvature increasing metric variations. Math. Ann. **276**, 633–641 (1987)

[10] Tapp, K.: Flats in Riemannian submersions from Lie groups. Asian J. Math. **13**, 459–464 (2009)

[11] Wilking, B.: Manifolds with positive sectional curvature almost everywhere. Invent. Math. **148**, 117–141 (2002)

[12] Ziller, W.: Examples of Riemannian manifolds with non-negative sectional curvature. In: Grove, K., Cheeger, J. (eds.) Metric and Comparison Geometry. Surveys in Differential Geometry, 11th edn, pp. 63–102. International Press, Somerville (2007)

Boris Stupovski and Rafael Torres
Scuola Internazionale Superiori di Studi Avanzati (SISSA)
Via Bonomea 265
34136 Trieste
Italy
e-mail: rtorres@sissa.it
e-mail: bstupovs@sissa.it

Received: 13 December 2019